

Revision 2

Petrogenesis of antecryst-bearing arc basalts from the Trans-Mexican Volcanic Belt: insights into along-arc variations in magma-mush ponding depths, H₂O contents, and surface heat flux

Georg F. Zellmer^{1,2*}, Mattia Pistone², Yoshiyuki Iizuka³, Benjamin J. Andrews², Arturo Gomez-Tuena⁴, Susanne M. Straub⁵, Elizabeth Cottrell²

¹Soil & Earth Sciences Group, IAE, Massey University, Palmerston North 4442, New Zealand

²National Museum of Natural History, Smithsonian Institution, Washington, DC 20560, USA

³Institute of Earth Sciences, Academia Sinica, 128 Academia Road Sec. 2, Nankang, Taipei 11529, Taiwan

⁴Centro de Geociencias, Universidad Nacional Autónoma de México, Querétaro 76230, Mexico

⁵Lamont-Doherty Earth Observatory of Columbia University, 61 Route 9W, Palisades, NY 10964, USA

*Corresponding author:

Phone: +64-6-951-7881

Fax: +64-6-350-5632

Email: g.f.zellmer@massey.ac.nz

35 **Abstract**

36 The Trans-Mexican Volcanic Belt (TMVB) is known for the chemical diversity in its erupted
37 products. We have analyzed the olivine, pyroxene and plagioclase mineral chemistry of 30
38 geochemically well-characterized mafic eruptives from Isla Maria at the western end of the arc to
39 Palma Sola in the east. The mineral major oxide data indicate the dominance of open system
40 processes such as antecryst uptake, and the scarcity of mineral-mineral and mineral-melt
41 equilibria suggests that erupted melts do not significantly crystallize during ascent. A
42 combination of plagioclase antecryst chemistry and MELTS thermodynamic modeling of H₂O-
43 saturated isobaric fractional crystallization was employed to develop a pressure sensor aimed at
44 determining the ponding depths of the co-genetic magmas from which the erupted plagioclase
45 crystal assemblage originates. We show that the depth of magma-mush reservoirs increase
46 eastwards along the TMVB. We suggest that magma ponding is triggered by degassing-induced
47 crystallization during magma ascent, and that the pressure sensor can also be regarded as a
48 degassing sensor, with more hydrous melts beginning to degas at greater depths. Modeled initial
49 magma H₂O contents at the Moho range from ~4 to ~9 wt%. Magma-mush ponding depth
50 variations fully explain the observed westward increase of average surface heat flux along the
51 TMVB, supporting a new model of mafic arc magma ascent, where rapidly rising, initially
52 aphyric melts pick up their antecrystic crystal cargo from a restricted crustal depth range, in
53 which small unerupted batches of previously risen co-genetic magmas typically stall and
54 solidify. This implies that globally, mafic arc magmas may be used to constrain the depths of
55 degassing and mush zone formation, as well as the amount of H₂O in the primary melts.

56 *Keywords: subduction, geobarometry, arc basalts, magma-mush zones, glomerocrysts, melt*
57 *ascent; hygrometry; degassing*

58

59 **Introduction**

60 Subduction zone magmatism is characterized by a wide range of melt compositions (basaltic
61 to rhyolitic, low-K to high-K), as well as eruption styles (explosive and effusive, VEI 0 to 8). A
62 variety of geophysical, petrological, geochemical, and modeling approaches have been pursued
63 to understand what parameters may control such a diversity. Towards the end of the last century,
64 primary melts were considered to be of mafic composition and originating from the mantle
65 wedge, with variable contributions of a slab signature (Gill, 1981; Thorpe, 1982). Melt
66 differentiation was attributed to magmatic processing within the overriding crust, and continental
67 arcs with thick crust showed the greatest degrees of melt evolution and isotopic indices of crustal
68 assimilation (Harmon et al., 1984; Hildreth and Moorbath, 1988). More recently, geochemical
69 variations in subcrustal primary melt compositions ranging between basalts and dacites have
70 been deduced, principally based on work on the Aleutians (Kelemen et al., 2003a; Kelemen et
71 al., 2003b; Yogodzinski et al., 1995; Yogodzinski et al., 2001) and the Trans-Mexican Volcanic
72 Belt (TMVB) (Gómez-Tuena et al., 2011; Gómez-Tuena et al., 2007b; Gómez-Tuena et al.,
73 2014; Petrone et al., 2003; Straub et al., 2011; Straub et al., 2013; Straub et al., 2014).

74 Understanding the processes of ascent of melts from their mantle source to the surface of the
75 overriding plate, as well as magma storage conditions within the overriding plate, is critical in
76 evaluating timescales of arc magmatism from generation to eruption and thus the potential
77 hazards from future volcanic eruptions, with repercussions for hazard mitigation strategies.
78 Magmatic processes are expected to depend on melt composition: mafic melts with low crystal
79 contents have a much lower viscosity than intermediate to silicic melts (Getson and Whittington,
80 2007; Giordano et al., 2008); furthermore, the viscosity of magmas, i.e. melts carrying a crystal

81 cargo, is strongly dependent on crystallinity (Caricchi et al., 2007; Lejeune and Richet, 1995),
82 melt H₂O content (Hess and Dingwell, 1996; Whittington et al., 2008), and vesicularity, i.e. the
83 presence or absence of exsolved magmatic gases (Pistone et al., 2013). Any study investigating
84 magma ascent processes and their links to the physical parameters such as subduction geometry,
85 slab age, convergence rate, and crustal thickness, should therefore focus on a tight compositional
86 range of eruptives in order to minimize the complicating additional effect of viscosity variations,
87 or take viscosity variations into account.

88 The TMVB lends itself to the study of the effect of physical parameters on magma ascent, as
89 there are significant along-arc variations in slab age (~3 to ~17 Ma at the trench), convergence
90 rate (~23 to 62 mm/yr), arc-trench distance (~150 to >400 km), and crustal thickness (~20-50
91 km), cf. Figure 1, which may variably influence the timescales and pathways of magma ascent.
92 This study investigates the petrogenetic and ascent processes of mafic magmas along the arc,
93 based on major oxide compositions of bulk rocks and their most abundant mineral phases
94 (olivine, pyroxene, and plagioclase). The petrography of samples is typical for mafic arc
95 magmas, displaying ample textural evidence for chemical disequilibrium. Our several thousand
96 mineral microanalyses show that conventional mineral-mineral and mineral-melt equilibria are
97 scarce in these basaltic samples, and that a simple concept of liquid lines of descent cannot be
98 usefully employed. Instead, we present a new magma ponding depth sensor based on plagioclase
99 compositions and isobaric MELTS modeling at a range of pressures. Using this "geobarometer",
100 we show that crystals found in mafic magmas record increasing magma ponding depths from
101 west to east along the arc. We propose that the depth of substantial crystallization, and thus mush
102 zone formation, is controlled by the onset of magma degassing during the ascent of initially
103 crystal-free, mantle-derived melts through the crust, with more hydrous melts in the eastern part

104 of the arc reaching H₂O-saturation at deeper levels. We derive H₂O contents of primitive melts
105 leaving the Moho at their liquidus, and compare these with previously published data from
106 hygrometry and olivine melt inclusion analysis. We also show that the observed ponding depth
107 variations are consistent with variations in average surface heat flux along the TMVB (Shapiro
108 and Ritzwoller, 2004), which is dominated by advected heat from ponding arc magmas (Zellmer
109 et al., 2015a). The methods applied in this study will lend themselves to investigations of mafic
110 arc magmas, including their crystal cargo and the volatile exsolution during their ascent, in other
111 subduction zones.

112

113 **Geological background and sample description**

114 The geological and tectonic history, as well as the magmatic diversity of the TMVB have
115 been discussed at length in previous studies (e.g., Ferrari et al., 2012; Gómez-Tuena et al.,
116 2007b; Manea et al., 2013), and are only briefly reviewed here (cf. Figure 1). Quaternary
117 volcanism is related to subduction at the Middle American Trench of the Rivera plate in the west
118 and the Cocos plate in the east. Convergence rates range from ~23 mm/yr in the west to ~62
119 mm/yr in the east (Bird, 2003). The age of the subducting slab at the trench ranges from ~3 Ma
120 in the west to ~17 Ma at the Orozco Fracture Zone. East of the fracture zone, the age increases
121 slightly from 14 Ma to 17 Ma. The volcanic arc is geographically divided into four sectors,
122 namely the western, central, eastern, and easternmost TMVB. Arc-trench distance increases
123 eastwards and exceeds 400 km in the easternmost TMVB due to flat-slab subduction in the
124 forearc (Pardo and Suarez, 1995). The crustal thickness of the overriding plate is highly variable,
125 ranging from 20 to 25 km at the western and eastern coastlines to over 50 km in parts of the
126 eastern TMVB (Ferrari et al., 2012, and references therein). The volcanic arc shows a wide range

127 of edifice morphologies, including monogenetic cinder cones, stratovolcanoes and caldera
128 structures. The chemistry of eruptive products is highly diverse, covering mafic to highly silicic
129 material with variable alkali contents ranging up to phonolitic compositions, although calc-
130 alkaline compositions dominate (Gómez-Tuena et al., 2007b).

131 The present study focuses on the whole-rock and mineral chemistry of mafic Mexican arc
132 samples taken along the entire length of the TMVB (see supplementary Figure S1 for a TAS
133 diagram). Sample details are provided in Table 1, and their geographic position is indicated in
134 Figure 1, which also shows the position of the dominant stratovolcanoes as well as crustal
135 thickness contours and the geodynamic context. Given the restricted compositional range of
136 mafic samples here considered, we cannot offer any constraints on the generation of tholeiitic
137 versus calc-alkaline trends. To evaluate such differentiation trends along the TMVB, we would
138 need to assess the degree of Fe-enrichment in more differentiated samples from individual
139 eruption centers, which is outside the scope of the present study. Whole-rock major oxide
140 contents of the mafic samples we studied are referenced in Table 1 and the data are compiled in
141 Table 2. In the western TMVB, we have studied samples from Isla Isabel (Housh et al., 2010),
142 the Mascota and the Amatlán de Cañas volcanic fields (Gómez-Tuena et al., 2011; Luhr et al.,
143 1989). On the boundary between the western and central TMVB, we have studied several
144 samples from the proximity of the Colima Volcanic Complex (Gómez-Tuena et al., 2011; Luhr
145 and Carmichael, 1981; Maria and Luhr, 2008; Verma and Luhr, 2010). In the central TMVB, we
146 include four samples from the Michoacán-Guanajuato volcanic field: one from Paricutín
147 (Hochstaedter et al., 1996), one from Jorullo (Luhr and Carmichael, 1985) near the arc front, and
148 two from the Valle de Santiago in the back-arc (Ortega-Gutiérrez et al., 2014). For the Paricutín
149 sample, Hochstaedter et al. (1996) do not provide all major oxides, and we have calculated its

150 composition by extrapolation of the mafic Paricutín trend (54.5-57 wt% SiO₂) of Cebria et al.
151 (2011) to the low silica content of this sample (52.5 wt%). In the eastern TMVB, we include two
152 samples from the Valle de Bravo-Zitácuaro volcanic field (Gómez-Tuena et al., 2007a); three
153 samples from the Chichinautzin volcanic field (Straub et al., 2013; Straub et al., 2014); and two
154 samples from the Serdan area (LaGatta, 2003). Finally, we have investigated four samples from
155 the Palma Sola volcanic field in the easternmost part of the arc (Gómez-Tuena et al., 2003). In
156 total, we have analyzed the mineral chemistry of 30 samples (Table 2), 28 of which are basalts,
157 trachybasalts, and basaltic andesites (Figure S1).

158

159 **Analytical Techniques**

160 Due to the scarcity of available samples, we did not produce standard thin sections for
161 optical microscopy, but restricted our study to microbeam analyses of polished thick sections.
162 Quantitative mineral chemical data were obtained by electron probe microanalyzer (EPMA) at
163 the Department of Mineral Sciences of the National Museum of Natural History, Smithsonian
164 Institution, Washington, DC, and at the Institute of Earth Sciences, Academia Sinica, Taipei,
165 Taiwan. The Smithsonian EPMA was a JEOL JXA-8900R probe equipped with five wavelength-
166 dispersive and one energy-dispersive spectrometers. Secondary- and backscattered electron
167 images were used to guide the analysis on target positions of minerals. A 2 µm defocused beam
168 was operated for analysis at an acceleration voltage of 15 kV with a beam current of 10 nA. Na,
169 Si, Mg, and Al were counted on TAP crystals for 20, 40, 20, and 40 s respectively; Ti and Ni on
170 LIF crystals for 10 and 50 s respectively; Ca and K on PET crystals for 40 s each; and Fe and Cr
171 on LIFH crystals for 30 and 50 s respectively. Upper and lower backgrounds were each counted
172 for half the amount of the peak counting times of each element.

173 The Academia Sinica probe used for quantitative microanalysis was a JEOL JXA-8900R
174 EPMA equipped with four wavelength-dispersive spectrometers. Acceleration voltage, beam
175 current, and beam diameter were identical to the conditions used at the Smithsonian. Counting
176 times for each element and both upper and lower backgrounds were 20 s and 10 s, respectively.

177 In both EPMAAs the measured X-ray intensities were corrected by the ZAF method using the
178 standard calibration of natural and synthetic standard minerals (Jarosewich et al., 1980).
179 Standards run as unknowns yielded relative standard deviations for Si, Na, and K of less than
180 1%, and less than 0.5% for other elements. Detection limits, based on 3σ of standard calibration,
181 were less than 500 ppm for all elements. Several samples were analyzed on both instruments and
182 yielded mineral chemical ranges for each sample that were identical within error.

183 Elemental distribution (mapping) analyses were performed at the Institute of Earth Sciences,
184 Academia Sinica, using a field emission electron probe micro analyzer (FE-EPMA: JEOL JXA-
185 8500F) equipped with five wave-length dispersive spectrometers. Beam conditions were 12 kV
186 and 10 nA for the acceleration voltage and beam current, respectively, using a 2 μm de-focused
187 beam. X-ray intensities were counted for 0.03 seconds at an interval of 2 μm with the X-Y stage
188 driving for a 10mm x 10mm area. Secondary- and back scattered electron images were used to
189 guide the analysis on the target area. Phenocryst proportions were estimated from the result of
190 elemental mapping analysis of Si, Ti, Fe, Ca and Na, deriving the modal abundances of
191 plagioclase and Fe-rich mineral phases, such as Fe-oxides, olivines, and pyroxenes, but
192 excluding microlites.

193

194 **Results**

195 *Petrography*

196 Most samples are fine grained. Throughout this contribution, we use the terms phenocryst and
197 microlite to refer to crystals larger than ~20-30 μm and less than ~20-30 μm in their shortest
198 dimension, respectively, initially without any petrogenetic connotation. Phenocryst proportions
199 are reported in Table 1 and are typically low, ranging from < 3 vol% to ~ 10 vol%, with only two
200 samples (MG05-13 and PS99-1) having ~ 15 vol% phenocrysts. With the exception of three
201 samples that are plagioclase-free (a trachybasalt, a basaltic trachyandesite, and a phonotephrite),
202 all rocks display an assemblage of olivine, pyroxene, and plagioclase, although in some these
203 phases are restricted to their microlite contents. Clinopyroxenes (i.e. augites) are ubiquitous with
204 the exception of one sample from Volcan Chichinautzin (sample S1) that instead contains
205 orthopyroxene. In other samples, orthopyroxenes are absent or rare, with the exception of three
206 samples (1004-500, J31, and S2), where orthopyroxenes range from 7% to about 45% of the
207 whole pyroxene population. Oxides such as magnetite and spinel are ubiquitous, as seen through
208 optical microscopy, but their crystal chemistry is not explored in this contribution. We also note
209 that no amphiboles are found in any of the samples we investigated.

210 BSE images of three samples are provided in Figure 2 to elucidate representative petrographic
211 features: the presence of glomerocrysts composed of olivine, pyroxene, Fe-oxides and
212 plagioclase is evident in some samples, cf. Figure 2a. Small glomerocrysts, including grains
213 made of only two crystals, as well as individual anhedral mafic crystals, some of microlitic size,
214 are seen in Figure 2b. In both of these cases, the groundmass is dominated by lath-shaped
215 microlites of plagioclase, with interdispersed anhedral to subhedral mafics. Figure 2c shows
216 larger crystals (200-400 μm) of magnesian olivine and of pyroxene set in a polyphase

217 groundmass. Phenocrysts range from subhedral to euhedral. Some pyroxenes display internal
218 zoning. The inset displays a grain consisting of pyroxene with some olivine at its edge. Figures
219 2d and 2e show Fe and Ca maps of sample with olivine and plagioclase set in a groundmass
220 dominated by microlites of low-Ca plagioclase and clinopyroxene. The interpretation of a broken
221 plagioclase crystal with a more calcic core that displays a slight concentric zonation is provided
222 in the inset of Figure 2d, while Figure 2e shows a more typical assemblage of crystals that are
223 unzoned or normally zoned with unzoned cores.

224

225 *Mineral chemistry*

226 The EPMA-based compositions of olivine, pyroxene, and plagioclase crystals are provided in
227 Supplementary Tables S1, S2, and S3, respectively. Although we have not explicitly
228 distinguished phenocryst cores and rims, the great majority of phenocryst analyses were taken
229 away from phenocryst rims, and overlap between phenocryst and microlite analyses described
230 below are therefore not an artefact of phenocryst rim analyses.

231 All samples are olivine-phyric, and compositions of olivine phenocrysts and microlites range
232 from F_{095} for the most primitive phenocrysts down to F_{036} for the most evolved microlites
233 (Figure 3). Within individual samples phenocrysts compositionally range between ~10 and ~30
234 units in forsterite content, and microlites show a similar range with few exceptions. None of the
235 samples have microlites more magnesian than their most magnesian phenocrysts, and generally
236 microlites compositionally overlap with the low-Mg phenocrysts and/or extend to less forsteritic
237 values than the phenocryst range. In a few cases (e.g. samples MAS15, JAL07-8A, PS99-3)
238 phenocrysts extend to lower forsterite contents than microlites. Further, compositional gaps in

239 phenocrysts and/or in microlites are seen in several samples (MAS21, JAL07-3B, J31, ZIT99-11,
240 SCI32B, and all Palma Sola samples).

241 The clinopyroxenes studied here display similarly wide crystal chemical variations: ranges of
242 Mg# (i.e. $Mg\# = 100 \times \text{molar Mg}/[Mg+Fe^{2+}]$) units of ~10 to > 30 are evident (Figure 4a), with
243 the total dataset spanning Mg# of 67-96 for phenocrysts and < 60-96 for microlites. Ca contents
244 in clinopyroxene are also variable. We have computed single-pyroxene temperatures at mid-
245 crustal levels (500 MPa, Figure 4b) after Lindsley (1983), noting that in the absence of
246 orthopyroxene in all but a few samples, these represent minimum temperatures, because at or
247 below the temperature of saturation a second pyroxene would be expected to form (Lindsley,
248 1983). While absolute temperatures are difficult to constrain, observed minimum temperature
249 ranges of ~200 °C and up to 500 °C are seen in the majority of samples. Such variations cannot
250 be attributed to differences in crustal formation pressures of these crystals, which would affect
251 temperatures only slightly (always less than 60 °C difference between 0.1 and 1500 MPa).
252 Strikingly, several samples show microlite temperatures at the upper end of the observed
253 temperature ranges, and in most samples phenocrysts record lower temperatures than the highest
254 temperatures recorded by the microlites.

255 Arguably the most diverse mineral chemistry is displayed by plagioclase crystals, again
256 within individual samples (Figure 5). Anorthite contents range from An₈₉ down to An₃₀ across
257 the entire sample set, with ranges of 20 to 50 anorthite units displayed by most samples. The
258 chemistry of phenocrysts and microlites overlaps significantly, and in some cases completely.
259 Several samples in addition to those with gaps in olivine compositions display distinct
260 compositional gaps in plagioclase phenocryst and/or microlite compositions. Despite these
261 striking compositional variations between crystals in each sample, however, a systematic

262 investigation of FE-EPMA elemental maps of all samples indicates that there are few exceptions
263 to individual plagioclase phenocrysts being unzoned or normally zoned with unzoned cores (cf.
264 Figure 2e). Finally, it is observed that the Mexican arc basalts do not contain plagioclase crystals
265 of An₉₀ or above, which typify hydrous subduction-related basaltic rocks in many other
266 locations. In fact, in several samples maximum anorthite contents of only ~An₇₀ or less are
267 observed.

268

269 **Discussion**

270 *Origin of the crystal cargo*

271 Historically, crystals carried by ascending magmas have been thought to form from their host
272 melt, and their separation from the melt (fractional crystallization) was taken as a means of the
273 chemical evolution of residual melts along liquid lines of descent (Bowen, 1928). In this
274 scenario, the expected observations are as follows: 1. Phenocrysts are euhedral, normally zoned,
275 their core to rim profiles serve as a recorder of closed system melt evolution along the liquid line
276 of descent (Hughes, 1982). 2. Phenocryst rims are in equilibrium with the host melt at all times
277 (Jerram and Martin, 2008). Disequilibria of earlier formed crystals in more evolved melts result
278 in peritectic reactions (cf. Zellmer et al., 2016). 3. Crystals forming solid solutions do not display
279 any compositional gaps (Vernon, 2004). 4. Microlite compositions are most evolved and
280 identical to the composition of the phenocryst rims (Jerram and Martin, 2008).

281 The above features are typical for closed system melt evolution, although more complex
282 petrographic textures characterized by skeletal and hopper crystals with complex or reverse
283 zoning have been described in systems that can be considered closed with exception of degassing
284 occurring during rapid melt ascent (Crabtree and Lange, 2011). However, it has long been

285 recognized that most arc magmas do not display strict closed-system petrographic features.
286 There is ample and clear evidence for open system processes, such as mineral-melt disequilibria
287 as evidenced by anhedral crystals with resorption zones, along with compositional gaps in the
288 solid solution compositions of phenocrysts, and occasionally accompanied by microlite-melt
289 disequilibria. These features are commonly attributed to magma mixing (e.g. Davidson et al.,
290 2000; Humphreys et al., 2009; Tepley et al., 1999), for which there is mesoscale evidence in
291 many arc eruptive products in the form of mafic enclaves within more evolved melts (e.g.,
292 Murphy et al., 1998; Zellmer et al., 2003; Zellmer and Turner, 2007), or mixing of magma with
293 crystal mush zones or cumulates (Pyle et al., 1988; Smith et al., 2010; Streck et al., 2007)
294 through processes of petrological cannibalism (Cashman and Blundy, 2013). Mixing of magmas
295 with variable compositions capable of introducing mineral-melt disequilibria should lead to
296 intermediate composition products (Kent et al., 2010). In the case of mafic products, such as the
297 Mexican arc samples here studied, mixing of mafic magmas is not expected to generate the
298 evolved crystal cargo observed in the rocks. Therefore magma-cumulate mixing is a more likely
299 scenario to introduce mineral-melt disequilibria, and is consistent with the occurrence of
300 glomerocrysts as seen in several samples (Figure 2). One end member of this open system
301 process is crystal uptake into aphyric arc melts, evidenced by several recent crystal chemical and
302 isotopic studies of mafic to intermediate arc eruptive products (Zellmer et al., 2014a; Zellmer et
303 al., 2015b; Zellmer et al., 2015c; Zellmer et al., 2014b). In this scenario, phenocrysts as well as
304 some of the microlites are the result of disintegration of larger glomerocrysts into smaller ones
305 and their subsequent breakup into individual subhedral grains (cf. Figures 2a, b). In some cases,
306 this process may not be as obvious, since some euhedral overgrowth masks anhedral to subhedral
307 crystal cores, and relicts of disintegration of a polyphase crystal mush are only found in a few

308 mineral grains (Figure 2c), while most glomerocrysts may have completely disintegrated. In the
309 sample shown in Figure 2c, the Fe-rich olivine rims are only seen in contact with the
310 groundmass, not in contact with pyroxene (cf. inset). This feature and the variably thick mantle
311 of the depicted grain suggest that it represents a remnant of a glomerocryst, rather than a case of
312 synneusis (Dowty, 1980; Vance, 1969; Vance and Gilreath, 1967), i.e. the merging of individual
313 crystals within the host melt. Disintegration of glomerocrysts into individual grains may be
314 accompanied by fragmentation of individual crystals (e.g. Figure 2d). While the growth of
315 phenocrysts from their host melt may well be a process operating in some scarcely phyrlic
316 intermediate composition melts from the western TMVB (Crabtree and Lange, 2011), all of the
317 above petrographic features suggest that the phenocrysts in the mafic rocks we sampled have not
318 crystallized from their host melt. In terms of petrogenetic processes, it appears then that mafic
319 arc magmas stall at depth, and the crystal cargo carried by the few mafic erupted melts is largely
320 assembled from earlier consanguineous crustal intrusions. In this case, crystals may be referred
321 to as antecrysts (Jerram and Martin, 2008), and the mineral chemical study of crystals from arc
322 eruptive products essentially targets the processes involved in the formation of the subvolcanic
323 intrusive suite of rocks. We note while many of the microlites may have crystallized from their
324 host melt during final magma ascent at the onset of the eruption, some may have formed by
325 disintegration of glomerocrysts and thus may not be in equilibrium with their host (cf. Figure 2,
326 and also see Humphreys et al., 2009).

327 In terms of mineral chemical variations, open system processes experienced by the mafic
328 melts erupted in the TMVB are evident in the significant compositional overlap of microlites and
329 phenocrysts, in the frequent occurrence of evolved phenocrysts in basaltic bulk rock
330 compositions, and in the existence of compositional gaps in phenocryst and/or microlite mineral

331 phase chemistries within individual samples. The lack of highly calcic plagioclase crystals
332 exceeding An₉₀, with maximum observed anorthite contents ranging between An₇₀ and An₈₃ for
333 most samples, and less than An₇₀ for some, indicates that none of the plagioclase phenocrysts
334 formed from H₂O-saturated mafic (i.e. Ca-rich) arc melts. The An# of Mexican bulk rocks
335 ranges from 38.0 to 65.4, with an average of 52.2 (Figure 6). Note that while Ca/Na ratios of
336 TMVB magmas are systematically lower than those of many oceanic arcs, this does not translate
337 into a straightforward concomitant lowering of the expected anorthite content of plagioclase
338 crystals forming from such melts at a given H₂O content, as can be demonstrated using the
339 plagioclase-liquid hygrometer of Waters & Lange (2015). Thus, the low plagioclase An contents
340 of many of the studied samples indeed require formation from more evolved magma
341 compositions, with liquid An contents from An₆₅ down to An₁₀₋₂₀ under H₂O-saturated
342 conditions (Waters and Lange, 2015, cf. Figure 6). In order to form in equilibrium with their host
343 melts, many of the plagioclase crystals should have nucleated and grown in equilibrium with
344 anhydrous melts. Yet, Mexican basalts clearly carry significant amounts of H₂O (1-7 wt%;
345 Cervantes and Wallace, 2003; Johnson et al., 2008; Johnson et al., 2009; Roberge et al., 2009;
346 Vigouroux et al., 2008), as expected for arc-related settings (Sisson and Layne, 1993; Ulmer,
347 2001). Thus, plagioclase formed from more evolved melts, which, given initially basaltic
348 compositions, would have acquired crystallinities of several tens of volume percent during their
349 differentiation. At crystallinities of ~40 vol%, the conditions of rheological lockup may be
350 achieved, and crystal mushes are formed (Bachmann and Bergantz, 2004). Therefore, we discuss
351 the petrogenesis of the studied Mexican arc samples with the following scenario in mind:
352 phenocrysts are “cannibalized” from cooling, co-genetic crystal mushes by initially aphyric,
353 hydrous basaltic melts during their ascent to the surface, i.e. they are antecrysts; most of the

354 microlites crystallize at shallow pressure (and thus low P_{H_2O}) in the melt phase of these melt-
355 mush mixtures.

356

357 *The An_{max} -MELTS pressure sensor*

358 Here we propose a novel ponding pressure sensor for basaltic systems, which is controlled by
359 i) composition and compositional variations of the crystal cargo as modeled by MELTS
360 (alphaMELTS 1.4, Ghiorso and Sack, 1995; Smith and Asimow, 2005), and ii) the relative
361 activities of the $CaAl_2Si_2O_8$ and $NaAlSi_3O_8$ components in the liquid through changes in the melt
362 Al_2O_3 and CaO availability, which, in turn, are reflected in the co-crystallizing plagioclase
363 compositions. When a rising melt batch stalls, it is fated to crystallize as it cools, and the
364 maximum An content in the resulting crystal mush is yielded by the first plagioclase crystal that
365 forms. Taking the TMVB whole-rocks as starting compositions, we first explored through
366 MELTS fractional crystallization modeling how the An content of the first plagioclase crystals
367 changes with pressure in initially H_2O -saturated mafic melts undergoing isobaric cooling (Figure
368 7, Figure S2). Given the presence of antecrystic crystal cargo, groundmasses would be more
369 suitable as starting compositions than bulk rocks, but for samples with low crystal contents (≤ 10
370 vol%), such as those we have studied here, whole-rock and groundmass compositions are
371 arguably very similar. All MELTS simulations were run at NNO+1, consistent with the oxygen
372 fugacities indicated by sulfur speciation of single melt inclusions and by Cr-spinel – olivine pairs
373 in the Mexican arc basalts (NNO+0.9 and NNO+1.3, with the exception of alkali basalts that
374 average NNO+0.5; Vigouroux et al., 2007; Vigouroux et al., 2008). Variations in oxygen
375 fugacity of ± 0.5 log units do not have a significant effect on the MELTS crystallization models

376 (cf. Figure S3a). Isobaric cooling of magmas ponding at specified depths was performed in 10°C
377 temperature steps.

378 In Figure 7 and Figure S2, maximum An contents predicted by MELTS modeling are plotted
379 against the modeled stalling pressure. At the shallowest pressures, An contents initially increase
380 as H₂O-saturated samples become more hydrous with increasing depth. The increase in An
381 content with increasing H₂O content has been discussed at length by Lange et al. (2009), and is
382 related to the partial dissolution of H₂O as hydroxyl groups, which increase the relative activity
383 of the CaAl₂Si₂O₈ component over the NaAlSi₃O₈ component in the liquid. The maximum
384 modeled An contents are reached between 50 and ~200 MPa H₂O-saturated pressure and range
385 from An₆₅ to An₈₀, depending on bulk composition.

386 Towards higher H₂O-saturated pressures in the lower crust, the maximum modeled An
387 content typically decreases, reaching values as low as An₅₀ in some samples. This is related to
388 the increasing H₂O content of H₂O-saturated samples at increasing pressures, resulting in a
389 contraction of the plagioclase stability field and early crystallization of more mafic Ca-rich
390 phases such as clinopyroxene. As pressure increases, plagioclase only becomes stable when the
391 residual melt is more evolved and already depleted in Ca. The profound influence of
392 clinopyroxene precipitation on the An content of plagioclase in solidifying gabbroic intrusions
393 has been previously recognized elsewhere (Namur et al., 2014).

394 In some samples, the smooth trends displayed by maximum An contents with increasing
395 pressures are interrupted due to complicating factors, such as coprecipitation of potassic feldspar,
396 which competes with plagioclase for aluminum, resulting in a ~30% drop in An content (Figures
397 7f and S2d-f), or coprecipitation of quartz at high pressure (Figure S2d), indicating high SiO₂
398 activity, which may favor the formation of alkali feldspar.

399 If the crystallinity of a sample is low (<10 vol%), and the composition of magmas erupted at
400 individual volcanic centers is representative of the composition of magmas in the TMVB at this
401 location, the initial, consanguineous mafic melt composition that formed the crystal cargo of
402 each sample will be similar to the bulk composition of the sample. Then, for each sample, the
403 maximum An contents predicted by the MELTS isobaric cooling models can be compared to the
404 observed ranges in An content in its actual plagioclase populations. On Figure 7 and Figure S2, it
405 is apparent that the An contents of plagioclase microlites range up to about the maximum An
406 predicted by the MELTS models at low pressures of 0.1-20 MPa in most samples, with the
407 exception of samples 1004-501, 109089, S1, PS99-22, and MG05-13. For the phenocrysts, we
408 have tied the maximum observed An contents to coincide with the MELTS models of the
409 respective bulk compositions, therefore obtaining an approximate formation pressure of the
410 phenocryst population of each sample. This An_{max} -MELTS pressure sensor allows the estimation
411 of an approximate storage pressure of the crystal mush zone from which the crystal cargo of the
412 studied sample was sourced (with uncertainties ranging from ± 30 to ± 200 MPa). Reasonable fits
413 are possible for most samples, with the exception of 1004-501, 109089, S1, PS99-22, and PS99-
414 20B, where the maximum observed An contents significantly exceed (by up to 5 An units) the
415 maximum An contents predicted by the respective MELTS models, and sample MG05-13, which
416 has a high crystal content and hosts several plagioclase populations (including megacrysts), thus
417 not resulting in a single, distinct pressure estimate. For these latter samples, the assumption of
418 similarity of initial melt and bulk composition may be violated. The An_{max} -MELTS pressure
419 sensor therefore cannot be applied to these samples.

420 The proposed An_{max} -MELTS pressure sensor presents several sources of uncertainty, which
421 we list here explicitly:

422 1. The MELTS starting composition may be dissimilar to the compositions from which the
423 plagioclase crystals have formed, as appears to be the case of the samples discussed above, so
424 that the modeled MELTS trends are not fully appropriate for the plagioclase populations studied.
425 Essentially, the assumption is made that the whole rock composition of the sample is
426 representative of the initial melt composition at the Moho, and that this composition is relatively
427 constant through time. Thus, the whole rock composition would also be representative of the
428 primitive melt from which the intrusive mush zone formed and where the plagioclase antecrysts
429 have their origin. By running MELTS models of selected groundmass compositions (calculated
430 on basis of mass balance, using average phenocryst compositions, cf. Figure S3b), we have
431 verified that the use of whole rock composition is appropriate for mafic samples with low
432 phenocryst contents (≤ 10 vol%), such as those we have studied (with exception of only two
433 samples; cf. Table 1). The approximate constancy of melt composition at any one point in the arc
434 is supported by the similarity of crystal contents, crystal chemistry, and whole rock composition
435 (as well as the resulting MELTS trend) erupted at an individual vent site, namely Tezontal in the
436 Colima Volcanic Complex, where all three samples (JAL07-2AB, SAY22E, SAY22F) are
437 similar on Figures 3, 4 and 5. We note that there are some exceptions in the literature (Carrasco-
438 Núñez et al., 2005; Petrone, 2010); however, the alkaline and calc-alkaline lavas from the El
439 Volcancillo vent in the eastern TMVB, for example, return strikingly similar pressures when the
440 An-MELTS sensor is applied to them (cf. Figure S4).

441 2. The MELTS code does not include a parameterization for amphibole, which is a controlling
442 mineral in many arc magmas, particularly at intermediate compositions (Caricchi and Blundy,
443 2016), although we note again that no amphiboles were detected in the samples studied here. The
444 lack of amphibole as a crystallizing phase in MELTS may not be fully appropriate. Instead of

445 amphibole, the crystallization of two pyroxenes is predicted, one non-aluminous and the other
446 aluminous. It is difficult to assess whether amphibole crystallization would affect melt major
447 oxide concentrations differently, and how this might impact the appearance and composition of
448 co-crystallizing plagioclase. However, we note that experimental melt composition is part of the
449 calibration of the MELTS model, and it is therefore likely that the appearance and composition
450 of plagioclase are not significantly affected. If amphiboles were part of the remobilized mush
451 assemblage, the high temperature of the mafic melt would have resulted in amphibole breakdown
452 to pyroxene and oxides (Krawczynski et al., 2012), which may be one reason for the lack of
453 amphiboles in our samples.

454 3. Uncertainties in plagioclase crystallization conditions likely increase during the
455 development of deep, evolved, and H₂O-rich magmas, which would be outside the experimental
456 calibration space of MELTS. We have tested the H₂O solubility model of MELTS on one of our
457 samples by comparison with the recent updated calibration of the plagioclase-liquid hygrometer-
458 thermometer, which is applicable to basalts through rhyolites (Waters and Lange, 2015) and has
459 been calibrated up to 8 wt% H₂O, and with the H₂O solubility model of Papale et al. (2006).
460 Figure 8 shows that up to ~7 wt% H₂O, MELTS predicts H₂O contents between these
461 hygrometry and solubility models, and thus may be reliable. Trends diverge above 250 MPa at
462 higher H₂O contents (> 7 wt%), but their relative and absolute reliability in this parameter space
463 cannot be assessed.

464 4. The pressure sensor assumes H₂O-saturated conditions at the onset of crystallization, which
465 may not be the case for all arc magmas. However, we note that in ascending arc magmas,
466 crystallization rate significantly increases during decompression-induced degassing, which
467 occurs upon H₂O saturation (Figure S5). With feldspar being late in the crystallizing assemblage,

468 H₂O saturation is likely when plagioclase enters the phase assemblage. Therefore, H₂O exsolves
469 during plagioclase crystallization in all MELTS runs.

470 5. The crystal population analyzed may not be large enough to identify the most anorthitic
471 plagioclase grains present (e.g. Figure S2j). Given the shape of the MELTS model curves in
472 Figure 7 and Figure S2, this would result in a slight pressure overestimate. However, as we use
473 the maximum observed An content, the determined pressures are minimum pressure limits, and
474 assume that the more sodic plagioclase crystals are formed as the mush zone differentiates with
475 time. An alternative scenario is that some of the more sodic crystals are formed at deeper levels.
476 Compositional gaps in An contents of individual samples may in fact point to several levels of
477 crystal mush formation and remobilization (see e.g., Figures S2o and S2r).

478 6. The uncertainty of the pressure sensor increases where the observed anorthite content
479 cannot be unequivocally tied to a specific pressure, i.e. where the slope of the MELTS model in
480 Figure 7 and Figure S2 is flat. This is typically the case at low, upper crustal pressures of ≤ 250
481 MPa.

482 Bearing the above-described uncertainties in mind, we now employ the An_{max}-MELTS
483 pressure sensor to assess potential mush remobilization pressures along the TMVB. Figure 9a
484 shows how the pressures determined through An_{max}-MELTS systematics vary along the TMVB.
485 The pressure sensor yields upper crustal pressures in the western TMVB, increasing through
486 mid-crustal pressures in the central TMVB to deep crustal pressures in the eastern part of the arc.
487 A basaltic andesite (S2) from Chichinautzin and a backarc sample (MG05-16B) from Valle de
488 Santiago were not included in the correlation because the former is more evolved than the other
489 samples and the latter is from the back arc. The correlation among the rest of the samples is
490 highly significant ($p < 0.0005$) and yields $R^2 = 0.87$. It thus appears that mush remobilization

491 depths broadly increase along the arc from 200 MPa in the east to 800 MPa in the west. We will
492 explore in the following why the depths of mush zone remobilization may vary so systematically
493 along the arc.

494

495 *A physical quantification of magma ascent and stalling*

496 Crystal mush formation and remobilization are likely intimately linked. Unlike fully solidified
497 plutons, mush zones are rheologically transient magmatic bodies, which can be defrosted during
498 reheating episodes (Burgisser and Bergantz 2011) and gas sparging (Bachmann and Bergantz,
499 2006) due to influx of new hot, volatile-rich magma (or exsolved volatiles), and therefore can
500 reach significant amounts of partial melt by defrosting the crystal framework (Huber et al.,
501 2010a; Huber et al., 2010b). We would therefore argue that the range in crystal mush
502 remobilization depths mirrors a similar range in preferred melt injection and magma ponding
503 depths.

504 It is necessary to explain along-arc depth variations of magma ponding, broadly increasing
505 towards the east of the TMVB arc. We propose that the initial H₂O content of rising magmas has
506 a profound effect. Water saturation and exsolution during melt ascent will occur at greater depths
507 for more hydrous magmas. If interconnected magma ascent pathways are present in the crustal
508 section, low-density hydrous melts will ascend very rapidly, closely following the adiabat; if not,
509 ascending melts are fated to stall. More hydrous melts may be expected to stall at deeper levels
510 for a number of reasons: 1. Degassing at depth will promote an increase in magma viscosity,
511 which is largely controlled by the volumetric proportions of exsolved gas, crystallinity, and the
512 residual melt and its polymerization (Pistone et al., 2013; Whittington et al., 2008). 2. Degassing
513 during adiabatic ascent may result in significant magma undercooling (Hammer and Rutherford,

514 2002; Pistone et al., 2016). Crystallization in response to undercooling can be much more
515 efficient than under equilibrium conditions, with ~40 vol% crystallinity resulting from an H₂O
516 loss of only 2 wt% (Pistone et al., 2016). 3. Ascent of hydrous melts in the deep crust is
517 characterized by thermal and chemical erosion of wall rocks, which widens existing conduits and
518 may form new ones (Bouilhol et al., 2015). Degassing will reduce the corrosiveness of the melts
519 and therefore promote their arrest at depth.

520 Adiabatic rise of initially aphyric melts, crystal uptake of stalling melts, as well as magma
521 ponding depths of the latter, here obtained through the An_{max}-MELTS pressure sensor, are
522 supported by important physical changes experienced by the decompressing magmas during their
523 ascent. We emphasize that viscosity is a major factor in determining the stalling of magmas at
524 depth, if degassing triggers magma crystallization. Strain rates within rapidly ascending basaltic
525 melts are high, and magmas are expected to have a pseudo-Binghamian rheology (e.g., Barnes,
526 1999; van der Werff et al., 1989). In this state, physical changes occur only through degassing,
527 which affects the melt viscosity by changing its H₂O content, and through crystallization, which
528 controls the magma (bulk) viscosity. In the light of recent rheological studies (e.g., Caricchi et
529 al., 2007; Picard et al., 2013; Pistone et al., 2012), to halt magma and induce its crystallization at
530 depth, a continuous solid framework must be generated (at only ~30 vol% crystals when tabular
531 plagioclase is the dominant phase; Picard et al., 2013), i.e. at < 2 wt% H₂O loss when the effect
532 of undercooling is considered (Pistone et al., 2016). This induces an increase of magma viscosity
533 by several orders of magnitude (Costa et al., 2009, and references therein) compared to the
534 viscosity of the original aphyric melt (< 13 Pa s, calculated using the model of Giordano et al.,
535 2008, cf. Table 5). Thus, the magma encounters a rheological barrier resulting from its sharp

536 viscosity increase (i.e. liquid to solid transition in Rosenberg and Handy, 2005, and references
537 therein) and will lock up and stall (Pistone et al., 2013).

538 Residual melt densities (estimated using the model of Lange and Carmichael, 1987; Table 5)
539 are relatively low (2100-2400 kg/m³). They will promote melt ascent, resulting in a volcanic
540 eruption if or when available magma ascent paths become available, e.g. through interconnection
541 of dikes. Interestingly, they also underline how ascending melts may preferentially take up
542 plagioclase crystals (with densities similar to those of rising mafic melts) over denser minerals
543 such as olivine and pyroxene (Scoates, 2000). This means that the phase proportions of the
544 antecrystic material within the basalts likely does not reflect mineral proportions in the mush
545 zone, which may be characterized by greater amounts of earlier crystallizing, mafic minerals.

546 In conclusion, our first order quantification of melt viscosity, and density quantification of
547 melts and magmas, support adiabatic rise of low-density aphyric melts, magmas then stalling
548 upon degassing, and crystal uptake by subsequent melts, and, therefore, can reasonably
549 corroborate the physical validity of the An_{max}-MELTS pressure sensor.

550

551 *Initial H₂O contents and degassing depths of rising melts*

552 Based on these considerations, we have modeled adiabatic ascent of melts with variable H₂O
553 contents from the Moho towards the surface using the MELTS algorithm (alphaMELTS 1.4,
554 Ghiorso and Sack, 1995; Smith and Asimow, 2005). Moho depths are constrained through
555 geophysical observations (Ferrari et al., 2012), and converted to Moho pressures using a suitable
556 depth-density model for the TMVB (Ortega-Gutiérrez et al., 2014, cf. Table 3). First, the melt
557 liquidus temperature was determined to 5 °C accuracy at the Moho (Table 3). The liquidus
558 temperature is dependent on melt chemistry and, above all, on H₂O content (Burnham and Jahns,

559 1962; Yoder et al., 1957), varying by ~ 100 °C for individual liquid compositions over the range
560 of H₂O contents investigated (< 2 to > 9 wt%). Second, the melt is adiabatically decompressed in
561 10 MPa steps towards the surface, and the pressure of initiation of degassing-induced
562 crystallization is determined from each MELTS run (Table 4). The H₂O content of the primary
563 melt is then modeled such that the pressure of degassing-induced crystallization coincides with
564 the An_{max}-MELTS pressure estimates (cf. Table 5). In this case, the An_{max}-MELTS pressure
565 sensor can also be used as a degassing sensor. Thus, the An_{max}-MELTS sensor can be employed
566 as a powerful tool to estimate the depth at which magmas degas and exsolved volatiles are
567 released.

568 Figure 9b shows how initial melt H₂O content increases from ~ 4 wt.% in western Mexico to
569 ~ 9 wt.% in the easternmost TMVB, and is well correlated with longitude ($p < 0.0005$, $R^2 = 0.74$)
570 when the backarc sample with low initial water content is excluded. Given that H₂O solubility
571 predicted by MELTS appears reliable up to ~ 7 wt.% (Figure 8), we are confident that the
572 modeled trend is not affected by potential problems in the MELTS parameterization. We note
573 that the highest modeled H₂O contents of Colima and Jorullo volcanoes correspond exceptionally
574 well with the highest H₂O content measured in olivine melt inclusions from these areas (6.2 and
575 5.7 wt%, respectively; Johnson et al., 2008; Vigouroux et al., 2008). Maximum olivine melt
576 inclusion H₂O contents in the Paricutín area reach 4.9 wt% (Johnson et al., 2009), close to the
577 values predicted by our line of best fit in Figure 9b. In the eastern TMVB, values of up to 5.2
578 wt% in the Chichinautzin region (Cervantes and Wallace, 2003) and 5.1% at Popocatepetl
579 (Roberge et al., 2009) plot below the range of modeled values. This is expected, given that melt
580 inclusion entrapment occurred at up to 400 MPa (Roberge et al., 2009), so that some magmatic
581 degassing will have taken place before inclusion formation, particularly in the eastern TMVB,

582 where our An_{\max} -MELTS sensor indicates ponding pressures of ≥ 500 MPa. Melt inclusion
583 entrapment in olivine likely occurs during melt ascent from these greater depths. West of
584 Colima, our model predicts relatively low H_2O contents of down to ~ 4 wt%. These are slightly
585 higher than those derived by plagioclase hygrometry (Lange et al., 2009) on mafic rocks from
586 around Tequila and Sangangüey volcanoes (≤ 4 wt%, Díaz-Bravo et al., 2014). We note,
587 however, that the suggested crystallization temperatures for these rocks of ~ 1240 to >1400 °C
588 are likely overestimates (cf. Table 5), given that the plagioclase crystals with highest An contents
589 do not form at the lower crustal pressures assumed by Díaz-Bravo et al. (cf. Figure 7). More
590 reasonable, lower temperatures prevalent during crystallization of the anorthitic plagioclase
591 crystals would produce slightly higher H_2O estimates consistent with our modeled trend.

592 What is the origin of increasing melt ponding pressures and, by inference, increasing initial
593 melt H_2O contents from west to east along the TMVB? We propose that the initial H_2O content
594 of the mafic magmas studied here is controlled by the amount of H_2O available at their source.
595 Water is released into the magma source region of subduction zones by dehydration of the
596 subducting slab (e.g., Tatsumi, 1989), and the H_2O content of a subducting slab increases with its
597 age due to continued hydration of the oceanic lithosphere by hydrothermal circulation of sea
598 water (e.g., Alt, 1995; Kelley et al., 2001). In Mexico, the age of the subducting slab at the trench
599 ranges from ~ 3 Ma at $106^\circ W$ to ~ 15 Ma at the Orozco fracture zone at $102^\circ W$, and then does not
600 significantly increase further eastwards (cf. Figure 1). However, the arc-trench distance, which is
601 roughly constant at ~ 200 km in the western to central TMVB, increases east of $102^\circ W$ to ~ 400
602 km in the easternmost TMVB due to flat slab subduction beneath the forearc (Manea et al.,
603 2013). It is thus expected that the age and H_2O content of the slab underneath the volcanic arc
604 continue to increase eastwards from $102^\circ W$. Further, there is no evidence for slab dehydration in

605 the forearc in Mexico: the geochemistry of hot springs found in the forearc region indicates
606 circulation of dominantly meteoric water, with little to no contribution from the subducting slab
607 (e.g., Inguaggiato et al., 2004; Ramírez-Guzmán et al., 2004; Taran et al., 2013). The low initial
608 H₂O content of the backarc sample (MG05-16B) is similarly expected due to slab dehydration
609 closer to the trench within the Michoacán-Guanajuato volcanic field, such that less water reaches
610 the backarc mantle wedge from which this sample is sourced.

611 Finally, the apparent transfer of increasing amounts of H₂O from slab to primary melts from
612 west to east along the arc implies that the degree of melting below the TMVB is not significantly
613 influenced by the H₂O content of the source, as has been suggested by Plank et al. (2013), but is
614 instead primarily governed by decompression melting (England and Katz, 2010), with H₂O
615 essentially being carried as a tracer of slab contributions.

616

617 *Effect of ponding depth variations on surface heat flux*

618 Compared to other continental arcs, the TMVB displays an extremely large along-arc
619 variation in surface heat flux, which decreases from high average values of ~150 mW/m² in the
620 west to more typical average values of ~80 mW/m² in the east (Shapiro and Ritzwoller, 2004, cf.
621 Table 5). Based on a global compilation of surface heat flux variations between 19 continental to
622 transitional arcs (Zellmer, 2008), the elevated heat flux values in western Mexico have been
623 suggested to result from shallower than typical magma ponding levels (Zellmer, 2009; Zellmer et
624 al., 2015a), a notion corroborated by the $A_{n_{max}}$ -MELTS pressure estimates presented in the
625 present study (Table 5, Figure 9a). Here, we use bilinear (latitude and longitude) interpolation of
626 the global surface heat flux model dataset (Shapiro and Ritzwoller, 2004) to constrain the surface
627 heat flux at the eruption sites of the mafic arc samples studied here. Figure 10a shows a good

628 correlation between average surface heat flux and ponding pressures inferred through the An_{max}-
629 MELTS pressure sensor ($p < 0.0005$, $R^2 = 0.80$). However, the total surface heat flux q is a
630 function of conductive heat flux q_{cd} from the Moho, radiogenic heat flux q_{rg} , and advected heat
631 flux q_{adv} from magmas intruding into the crust, namely:

$$632 \quad q = q_{cd} + q_{rg} + q_{adv}.$$

633 It is expected that the advected component of the surface heat flux would be better correlated
634 with magma ponding pressures than the total surface heat flux. To test this hypothesis, we have
635 calculated the advected component as follows: we note that the background cratonic heat flux
636 away from subduction zones is ~ 40 mW/m² (Shapiro and Ritzwoller, 2004), out of which ~ 25
637 mW/m² are attributable to radiogenic heat production (Pollack, 1982). We therefore infer that the
638 conductive heat flux q_{cd} across the average cratonic crustal thickness of ~ 40 km (Bassin et al.,
639 2000; Mooney et al., 1998) is ~ 15 mW/m². The expected background surface heat flux q_{bkg} as a
640 function of crustal thickness can therefore be calculated as:

$$641 \quad q_{bkg} = q_{rg} + q_{cd} * (1111 \text{ MPa})/P_{\text{Moho}},$$

642 where P_{Moho} is the pressure at the Moho and we are using the crustal density structure as
643 indicated in Table 3 (where 1111 MPa is the pressure at 40 km depth). The advected component
644 of the total heat flux is then simply derived by subtracting the background heat flux from the
645 total observed heat flux:

$$646 \quad q_{adv} = q - q_{bkg}.$$

647 Figure 10b shows that the correlation of this advected component of the surface heat flux with
648 ponding pressure is indeed significantly improved and excellent ($p < 0.0005$, $R^2 = 0.92$). We take
649 this as evidence for the profound effect of magma ponding level on surface heat flux, as well as
650 providing strong support for the reliability of the An_{max}-MELTS pressure sensor introduced as

651 part of this study and the overall model of magma ascent, ponding, mush remobilization and
652 eruption at the TMVB applied here. The correlations also corroborate the notion that H₂O
653 degassing and the resulting crystallization exerts a primary control on the stalling of magmas
654 during their ascent through the crust.

655 Finally, we note that the backarc sample (MG05-16B) plots well below the along-arc trend,
656 suggesting that its shallow ponding depth is not representative for the backarc. The other Valle
657 de Santiago sample we have studied (MG05-13) is the most phenocryst-rich sample of this study,
658 and contains multiple crystal populations (including megacrysts) with low anorthite contents of
659 An_{<57} for most crystals. We do not trust the An_{max}-MELTS pressure sensor for this sample, as
660 microlite anorthite contents plot well below the bulk-rock MELT model predictions for 0.1 MPa
661 (cf. Figure S2r). However, the lower anorthite contents of most of its plagioclase crystals relative
662 to sample MG05-16B (Figure 5) may point to a deeper origin of its crystal cargo. Initial melt
663 H₂O contents in the back arc may be more variable than at the arc front, resulting in a greater
664 depth range of degassing-induced mush zone formation and remobilization. More back-arc
665 samples will have to be considered to assess such variations.

666

667 **Summary**

668 This along-arc study of plagioclase-phyric basalts of the TMVB has shown that:

- 669 1. The petrography and mineral chemistry of eruptives along the arc reflects open system
670 processes that dominate the petrogenesis of erupted melts, with ubiquitous evidence for
671 glomerocryst disintegration and crystal uptake into initially aphyric arc melts.
- 672 2. A new pressure sensor can constrain crystallization pressures of plagioclase antecrysts
673 from mush zones that are remobilized by mafic arc melts during their ascent to the

674 surface. These antecrysts have formed during ponding (at the onset of degassing) and
675 crystallization of melts with similar initial composition as their present host melt. The
676 pressure sensor is based on a combination of plagioclase An content and the whole-rock
677 composition of the mafic carrier melt, as well as its evolution modeled using the MELTS
678 algorithm. It assumes that melt compositions leaving the mantle wedge are approximately
679 constant at a given location within volcanic arc; that melt composition is approximated
680 by the whole rock composition of the sample; and that plagioclase crystallization occurs
681 under H₂O saturated conditions. In this contribution, we have provided evidence that
682 supports the applicability of these assumptions.

683 3. Plagioclase crystallization depths as determined through the An_{max}-MELTS pressure
684 sensor increase from west to east along the TMVB. This suggests that the level of crystal
685 mush zones that are the source of those plagioclase crystals increases in the same fashion
686 and that the depth of magma ponding levels increase eastwards.

687 4. The initial magmatic H₂O contents increase along the TMVB from ~ 4wt% in the west to
688 ~ 9 wt% in the east, consistent with the eastwards increasing age of the subducted slab
689 beneath the volcanic arc. H₂O contents measured in olivine melt inclusions are minimum
690 values (cf. Gaetani et al., 2012), and as such are not inconsistent with those modeled
691 concentrations.

692 5. The observed westward increase in surface heat flux is the result of increasing advected
693 heat flux by unerupted melt batches, which reach shallower crustal ponding levels in the
694 west of the TMVB.

695 6. Strikingly, variations in crustal thickness along the TMVB (cf. Figure 1) do not appear to
696 have any direct influence on the depths of degassing, magma-mush zone formation, and

697 crystal uptake, despite the clear effect of crustal thickness on bulk rock compositions in
698 subduction zones globally (Plank and Langmuir, 1988; Turner and Langmuir, 2015a;
699 Turner and Langmuir, 2015b).

700 Figure 11 depicts the petrogenetic model of the magmatic processes that we infer to operate
701 along the TMVB on basis of this study.

702

703 **Implications**

704 The primary implication of the work presented here is that mafic arc magmas can be used to
705 infer the onset of degassing and stalling of ascending melts feeding magma-mush reservoirs in
706 subduction zones. Magmas are generated in the mantle wedge through decompression-induced
707 melting, and carry a variable amount of water as part of their slab signature. Small batches of
708 H₂O-undersaturated mafic magmas leave the base of the crust at their liquidus and migrate
709 adiabatically upwards through a network of melt channels. Mafic melt crystallization is fostered
710 by decompression-induced degassing once melts reach H₂O saturation. Degassing-induced
711 crystallization increases magma viscosity, promoting stalling, slow cooling, and phenocryst
712 growth, which may clog melt migration pathways. Therefore, magma ponding preferentially
713 occurs at levels where degassing-induced crystallization sets in: more hydrous, cooler melts
714 reach volatile saturation (and therefore stall) at greater depths. Upon stalling, the water-saturated
715 small melt batches cool and form crystal mushes with evolved and hydrous interstitial melts
716 (Figure 11). In the deep crust, crystallization of clinopyroxene decreases melt Ca-contents such
717 that delayed feldspar crystallization produces more sodic plagioclase crystals than at the
718 shallower depths reached by initially less hydrous melts. Plagioclase An contents peak at mid- to
719 shallow crustal levels, between 50 and ~200 MPa, depending on melt composition. Finally,

720 erupted mafic melts are of similar composition to magmas parental to the co-genetic mush zones,
721 established by concomitant intrusive magmatism, and preferentially pick up crystals from those
722 mush zones to bring them to the surface. Eruption only occurs when magma ascent pathways are
723 readily available. If not, degassing-induced crystallization results in the stalling of magmas at
724 depth (Figure 11).

725 We propose that this mafic arc magma transfer model may be applied to other arcs and, when
726 combined with surface heat flux constraints from other arcs, will provide some insights into the
727 global intrusive magma budget at subduction zones. The plagioclase pressure sensor developed
728 here may in future be employed at different localities. We stress that its use should be restricted
729 to hydrous mafic samples (i.e. arc basalts and trachybasalts or low-SiO₂ arc basaltic andesites)
730 that carry antecrysts and that are (i) either very sparsely phyrlic with ≤ 10 vol% of large crystals,
731 or (ii) alternatively well characterized in terms of their groundmass major oxide composition. We
732 caution that its application to anhydrous systems or to more evolved compositions (e.g. our
733 samples S1 and S2) or antecryst-free rocks (cf. Crabtree and Lange, 2011) will not yield reliable
734 results, and that its application to backarc samples needs to be tested further.

735

736 **Acknowledgments**

737 Leslie Hale provided valuable on-site help in identifying relevant samples from Jim Luhr's
738 Mexican Volcanic Belt collection of the National Museum of Natural History of the Smithsonian
739 Institution. We are indebted to Hui-Ho Hsieh from Academia Sinica and Timothy Gooding and
740 Timothy Rose from the National Museum of Natural History for valuable assistance with sample
741 preparation and microprobe analysis. We thank Laura Waters for early access to the recently
742 published plagioclase-liquid hygrometer-thermometer. This contribution benefitted from

743 constructive input by John Adam, Mark Bebbington, Fred Davis, Szabolcs Kósik, and Laura
744 Waters, and from thoughtful reviews by Scott Bryan and Chiara Petrone. GFZ acknowledges a
745 Smithsonian Institution visiting fellowship for February-July 2013 and July 2015, funded
746 through the Smithsonian Institution – Global Volcanism Program (<http://volcano.si.edu/>), and
747 travel support by Massey University.

748

749

750 **References**

- 751 Alt, J.C. (1995) Subseafloor processes in mid-ocean ridge hydrothermal systems. In S.E.
752 Humphris, R. Zierenberg, L.S. Mullineaux, and R.E. Thomson, Eds. Seafloor
753 hydrothermal systems: physical, chemical, biological, and geological interactions, 91, p.
754 85-114. AGU Geophysical Monograph Series.
- 755 Bachmann, O., and Bergantz, G.W. (2004) On the origin of crystal-poor rhyolites: Extracted
756 from batholithic crystal mushes. *Journal of Petrology*, 45(8), 1565-1582.
- 757 -. (2006) Gas percolation in upper-crustal silicic crystal mushes as a mechanism for upward heat
758 advection and rejuvenation of near-solidus magma bodies. *Journal of Volcanology and*
759 *Geothermal Research*, 149(1-2), 85-102.
- 760 Barnes, H. (1999) The yield stress – a review or ‘παντα ρει’—everything flows? *Journal of Non-*
761 *Newtonian Fluid Mechanics*, 81, 133-178.
- 762 Bassin, C., Laske, G., and Masters, T.G. (2000) The current limits of resolution for surface wave
763 tomography in North America. *EOS Trans. AGU*, 81, F897. Available at
764 <http://mahi.ucsd.edu/Gabi/rem.html>.
- 765 Bird, P. (2003) An updated digital model of plate boundaries. *Geochemistry Geophysics*
766 *Geosystems*, 4, 1-52.
- 767 Bouilhol, P., Schmidt, M.W., and Burg, J.-P. (2015) Magma transfer and evolution in channels
768 within the arc crust: the pyroxenitic feeder pipes of Sapat (Kohistan, Pakistan). *Journal of*
769 *Petrology*, 56, 1309-1342.
- 770 Bowen, N.L. (1928) *The evolution of the igneous rocks*. Princeton University Press, Princeton.
- 771 Burgisser, A., and Bergantz, G.W. (2011) A rapid mechanism to remobilize and homogenize
772 highly crystalline magma bodies. *Nature*, 471, 212-215.
- 773 Burnham, C.W., and Jahns, R.H. (1962) A method for determining the solubility of water in
774 silicate melts. *American Journal of Science*, 260, 721-745.
- 775 Caricchi, L., and Blundy, J. (2016) The temporal evolution of chemical and physical properties
776 of magmatic systems. In L. Caricchi, and J. Blundy, Eds. *Chemical, physical and*
777 *temporal evolution of magmatic systems*. Geological Society, London, Special
778 *Publications*, 422, p. 1-15.
- 779 Caricchi, L., Burlini, L., Ulmer, P., Gerya, T., Vassalli, M., and Papale, P. (2007) Non-
780 Newtonian rheology of crystal-bearing magmas and implications for magma ascent
781 dynamics. *Earth and Planetary Science Letters*, 264, 402-419.
- 782 Carrasco-Núñez, G., Richter, K., Chesley, J., Siebert, L., and Aranda-Gómez, J.J. (2005)
783 Contemporaneous eruption of calc-alkaline and alkaline lavas in a continental arc
784 (Eastern Mexican Volcanic Belt): chemically heterogeneous but isotopically
785 homogeneous source. *Contributions to Mineralogy and Petrology*, 150, 423-440.
- 786 Cashman, K., and Blundy, J. (2013) Petrological cannibalism: the chemical and textural
787 consequences of incremental magma body growth. *Contributions to Mineralogy and*
788 *Petrology*, 166, 703-729.
- 789 Cebriá, J.M., Martiny, B.M., López-Ruiz, J., and Moraán-Zenteno, D.J. (2011) The Parícutin
790 calc-alkaline lavas: New geochemical and petrogenetic modelling constraints on the
791 crustal assimilation process. *Journal of Volcanology and Geothermal Research*, 201, 113-
792 125.

- 793 Cervantes, P., and Wallace, P.J. (2003) Role of H₂O in subduction-zone magmatism: New
794 insights from melt inclusions in high-Mg basalts from central Mexico. *Geology*, 31, 235–
795 238.
- 796 Costa, A., Caricchi, L., and Bagdassarov, N. (2009) A model for the rheology of particle-bearing
797 suspensions and partially molten rocks. *Geochemistry Geophysics Geosystems*, 10, 1-13.
- 798 Crabtree, S.M., and Lange, R.A. (2011) Complex phenocryst textures and zoning patterns in
799 andesites and dacites: evidence of degassing-induced rapid crystallization? *Journal of*
800 *Petrology*, 52, 3-38.
- 801 Davidson, J., Tepley, F., Palacz, Z., and Meffan-Main, S. (2000) Magma recharge,
802 contamination and residence times revealed by in situ laser ablation isotopic analysis of
803 feldspar in volcanic rocks. *Earth and Planetary Science Letters*, 184, 407-442.
- 804 Díaz-Bravo, B.A., Gómez-Tuena, A., Ortega-Obregón, C., and Pérez-Arvizu, O. (2014) The
805 origin of intraplate magmatism in the western Trans-Mexican Volcanic Belt. *Geosphere*,
806 10, 340-373.
- 807 Dowty, E. (1980) Synneusis reconsidered. *Contributions to Mineralogy and Petrology*, 74, 75-
808 84.
- 809 England, P.C., and Katz, R.F. (2010) Melting above the anhydrous solidus controls the location
810 of volcanic arcs. *Nature*, 467, 700-703.
- 811 Ferrari, L., Orozco-Esquivel, T., Manea, V., and Manea, M. (2012) The dynamic history of the
812 Trans-Mexican Volcanic Belt and the Mexico subduction zone. *Tectonophysics*, 522-523,
813 122-149.
- 814 Gaetani, G.A., O'Leary, J.A., Shimizu, N., Bucholz, C.E., and Newville, M. (2012) Rapid
815 reequilibration of H₂O and oxygen fugacity in olivine-hosted melt inclusions. *Geology*,
816 40, 915-918.
- 817 Getson, J.M., and Whittington, A.G. (2007) Liquid and magma viscosity in the anorthite-
818 forsterite-diopside-quartz system and implications for the viscosity-temperature paths of
819 cooling magmas. *Journal of Geophysical Research*, 112.
- 820 Ghiorso, M.S., and Sack, R.O. (1995) Chemical mass transfer in magmatic processes IV. A
821 revised and internally consistent thermodynamic model for the interpolation and
822 extrapolation of liquid-solid equilibria in magmatic systems at elevated temperatures and
823 pressures. *Contributions to Mineralogy and Petrology*, 119, 197-212.
- 824 Gill, J.B. (1981) *Orogenic andesites and plate tectonics*. Springer Verlag, Heidelberg.
- 825 Giordano, D., Russell, J.K., and Dingwell, D.B. (2008) Viscosity of magmatic liquids: a model.
826 *Earth and Planetary Science Letters*, 271, 123-134.
- 827 Gómez-Tuena, A., LaGatta, A.B., Langmuir, C.H., Goldstein, S.L., Ortega-Gutiérrez, F., and
828 Carrasco-Núñez, G. (2003) Temporal control of subduction magmatism in the eastern
829 Trans-Mexican Volcanic Belt: Mantle sources, slab contributions, and crustal
830 contamination. *Geochemistry Geophysics Geosystems*, 4(8), 8912.
- 831 Gómez-Tuena, A., Langmuir, C.H., Goldstein, S.L., Straub, S.M., and Ortega-Gutierrez, F.
832 (2007a) Geochemical evidence for slab melting in the trans-Mexican volcanic belt.
833 *Journal of Petrology*, 48(3), 537-562.
- 834 Gómez-Tuena, A., Mori, L., Goldstein, S.L., and Pérez-Arvizu, O. (2011) Magmatic diversity of
835 western Mexico as a function of metamorphic transformations in the subducted oceanic
836 plate. *Geochimica et Cosmochimica Acta*, 75, 213-241.

- 837 Gómez-Tuena, A., Orozco-Esquivel, M.T., and Ferrari, L. (2007b) Igneous petrogenesis of the
838 Trans-Mexican Volcanic Belt. Geological Society of America Special Papers,
839 422(spe422-05), 53 pages.
- 840 Gómez-Tuena, A., Straub, S.M., and Zellmer, G.F. (2014) An introduction to orogenic andesites
841 and crustal growth. In A. Gómez-Tuena, S.M. Straub, and G.F. Zellmer, Eds. Orogenic
842 andesites and crustal growth, 385, p. 1-13. Geological Society, London, Special
843 Publications.
- 844 Hammer, J.E., and Rutherford, M.J. (2002) An experimental study of the kinetics of
845 decompression-induced crystallization in silicic melt. Journal of Geophysical Research,
846 107(B1), 2021.
- 847 Harmon, R.S., Barreiro, B.A., Moor bath, S., Hoefs, J., Francis, P.W., Thorpe, R.S., Duruelle, B.,
848 McHugh, J., and Viglino, J.A. (1984) Regional O-, Sr-, and Pb- isotope relationships in
849 the late Cenozoic calc-alkaline lavas of the Andean Cordillera. Journal of the Geological
850 Society of London, 141, 803-822.
- 851 Hess, K., and Dingwell, D.B. (1996) Viscosities of hydrous leucogranitic melts: A non-
852 Arrhenian model. American Mineralogist, 81, 1297-1300.
- 853 Hildreth, W., and Moor bath, S. (1988) Crustal contribution to arc magmatism in the Andes of
854 Central Chile. Contributions to Mineralogy and Petrology, 98, 455-489.
- 855 Hochstaedter, A.G., Ryan, J.G., Luhr, J.F., and Hasenaka, T. (1996) On B/Be ratios in the
856 Mexican Volcanic Belt. Geochimica et Cosmochimica Acta, 60, 613-628.
- 857 Housh, T.B., Aranda-Gómez, J.J., and Luhr, J.F. (2010) Isla Isabel (Nayarit, México):
858 Quarternary alkalic basalts with mantle xenoliths erupted in the mouth of the Gulf of
859 California. Journal of Volcanology and Geothermal Research, 197, 85-107.
- 860 Huber, C., Bachmann, O., and Dufek, J. (2010a) Thermo-mechanical reactivation of locked
861 crystal mushes: Melting-induced internal fracturing and assimilation processes in
862 magmas. Earth and Planetary Science Letters, 304, 443-454.
- 863 Huber, C., Bachmann, O., and Manga, M. (2010b) Two competing effects of volatiles on heat
864 transfer in crystal-rich magmas: Thermal insulation vs defrosting. Journal of Petrology,
865 51, 847-867.
- 866 Hughes, C.J. (1982) Igneous Petrology. xvi + 551 p. Elsevier Scientific Publishing Co.,
867 Amsterdam, Oxford, New York.
- 868 Humphreys, M.C.S., Christopher, T., and Hards, V. (2009) Microlite transfer by disaggregation
869 of mafic inclusions following magma mixing at Soufrière Hills volcano, Montserrat.
870 Contributions to Mineralogy and Petrology, 157, 609-624.
- 871 Inguaggiato, S., Taran, Y., Grassa, F., Campasso, G., Favara, R., Varley, N., and Faber, E.
872 (2004) Nitrogen isotopes in thermal fluids of a forearc region (Jalisco Block, Mexico):
873 Evidence for heavy nitrogen from continental crust. Geochemistry Geophysics
874 Geosystems, 5, Q12003.
- 875 Jarosewich, E.J., Nelen, J.A., and Norberg, J.A. (1980) Reference samples for electron
876 microprobe analyses. Geostandards Newsletter, 4, 43-47.
- 877 Jerram, D.A., and Martin, V.M. (2008) Understanding crystal populations and their significance
878 through the magma plumbing system. In C. Annen, and G.F. Zellmer, Eds. Dynamics of
879 crustal magma transfer, storage and differentiation, 304, p. 133-148. Geological Society,
880 London.
- 881 Johnson, E.R., Wallace, P.J., Cashman, K.V., Delgado Granados, H., and Kent, A.J.R. (2008)
882 Magmatic volatile contents and degassing-induced crystallization at Volcán Jorullo,

- 883 Mexico: Implications for melt evolution and the plumbing systems of monogenetic
884 volcanoes. *Earth and Planetary Science Letters*, 269, 478-487
- 885 Johnson, E.R., Wallace, P.J., Delgado-Granados, H., Manea, V.C., Kent, A.J.R., Bindeman, I.N.,
886 and Donegan, C.S. (2009) Subduction-related volatile recycling and magma generation
887 beneath central Mexico: insights from melt inclusions, oxygen isotopes and geodynamic
888 models. *Journal of Petrology*, 50(9), 1729-1764.
- 889 Kelemen, P.B., Hanghoj, K., and Greene, A.R. (2003a) One view of the geochemistry of
890 subduction-related magmatic arcs, with an emphasis on primitive andesite and lower
891 crust. In H.D. Holland, and K.K. Turekian, Eds. *Treaties on Geochemistry*, 3, p. 593–
892 659. Elsevier, Amsterdam.
- 893 Kelemen, P.B., Yogodzinski, G.M., and Scholl, D.W. (2003b) Along-strike variation in lavas of
894 the Aleutian island arc: implications for the genesis of high-Mg# andesite and the
895 continental crust. In J. Eiler, Ed. *Inside the subduction factory*. American Geophysical
896 Union. *Geophysical Monograph*, 138, p. 223-274.
- 897 Kelley, D.S., Karson, J.A., Blackman, D.K., Früh-Green, G.L., Butterfield, D.A., Lilley, M.D.,
898 Olson, E.J., Schrenk, M.O., Roe, K.K., Lebon, G.T., Rivizzigno, P., and Party, A.-S.
899 (2001) An off-axis hydrothermal vent field near the Mid-Atlantic Ridge at 30° N. *Nature*,
900 412, 145-149.
- 901 Kent, A.J.R., Darr, C., Koleszar, A.K., Salisbury, M.J., and Cooper, K.M. (2010) Preferential
902 eruption of andesite magmas through recharge filtering. *Nature Geoscience*, 3, 631-636.
- 903 Kohut, E.J., and Nielsen, R.L. (2003) Low-pressure phase equilibria of anhydrous anorthite-
904 bearing mafic magmas. *Geochemistry Geophysics Geosystems*, 4(7), 1057.
- 905 Krawczynski, M.J., Grove, T.L., and Behrens, H. (2012) Amphibole stability in primitive arc
906 magmas: effects of temperature, H₂O content, and oxygen fugacity. *Contributions to
907 Mineralogy and Petrology*, 164, 317-339.
- 908 LaGatta, A.B. (2003) Arc magma genesis in the eastern Mexican Volcanic Belt. PhD thesis, p.
909 329. Columbia University.
- 910 Lange, R.A., and Carmichael, I.S.E. (1987) Densities of Na₂O-K₂O-MgO-MgO-FeO-Fe₂O₃-
911 Al₂O₃-TiO₂-SiO₂ liquids: New measurements and derived partial molar properties.
912 *Geochimica et Cosmochimica Acta*, 51(11), 2931-2946.
- 913 Lange, R.A., Frey, H.M., and Hector, J. (2009) A thermodynamic model for the plagioclase-
914 liquid hygrometer/thermometer. *American Mineralogist*, 94, 494-506.
- 915 Lejeune, A., and Richet, P. (1995) Rheology of crystal-bearing silicate melts: An experimental
916 study at high viscosity. *Journal of Geophysical Research*, 100, 4215–4229.
- 917 Lindsley, D.H. (1983) Pyroxene thermometry. *Am. Mineral.*, 68, 477-493.
- 918 Luhr, J.F., Allan, J.F., Carmichael, I.S.E., Nelson, S.A., and Hasenaka, T. (1989) Primitive calc-
919 alkaline and alkaline rock types from the western Mexican Volcanic Belt. *Journal of
920 Geophysical Research*, 94(B4), 4515-4530.
- 921 Luhr, J.F., and Carmichael, I.S.E. (1981) The Colima Volcanic Complex, Mexico: Part II. Late-
922 Quaternary cinder cones. *Contributions to Mineralogy and Petrology*, 76, 127-147.
- 923 -. (1985) Jorullo Volcano, Michoacan, Mexico (1759-1774): the earliest stages of fractionation in
924 calc-alkaline magmas. *Contributions to Mineralogy and Petrology*, 90, 142-161.
- 925 Manea, V.C., Manea, M., and Ferrari, L. (2013) A geodynamical perspective on the subduction
926 of Cocos and Revera plates beneath Mexico and Central America. *Tectonophysics*, 609,
927 56-81.

- 928 Maria, A.H., and Luhr, J.F. (2008) Lamprophyres, basanites, and basalts of the Western Mexican
929 Volcanic Belt: volatile contents and a vein-wallrock melting relationship. *Journal of*
930 *Petrology*, 49, 2123-2156.
- 931 Mooney, W.D., Laske, G., and Masters, T.G. (1998) Crust 5.1: a global crustal model at 5x5
932 degrees. *Journal of Geophysical Research*, 103, 727-747.
- 933 Murphy, M.D., Sparks, R.S.J., Barclay, J., Carroll, M.R., Lejeune, A.-M., Brewer, T.S.,
934 Macdonald, R., Black, S., and Young, S. (1998) The role of magma mixing in triggering
935 the current eruption at the Soufriere Hills volcano, Montserrat, West Indies. *Geophysical*
936 *Research Letters*, 25, 3433-3436.
- 937 Namur, O., Humphreys, M.C.S., and Holness, M.B. (2014) Crystallization of interstitial liquid
938 and latent heat buffering in solidifying gabbros: Skaergaard intrusion, Greenland. *Journal*
939 *of Petrology*, 55, 1389-1427.
- 940 Ortega-Gutiérrez, F., Gómez-Tuena, A., Elías-Herrera, M., Solari, L.A., Reyes-Salas, M., and
941 Macías-Romo, C. (2014) Petrology and geochemistry of the Valle de Santiago lower-
942 crust xenoliths: Young tectonothermal processes beneath the central Trans-Mexican
943 volcanic belt. *Lithosphere*, in press.
- 944 Papale, P., Moretti, R., and Barbato, D. (2006) The compositional dependence of the saturation
945 surface of H₂O + CO₂ fluids in silicate melts. *Chemical Geology*, 229, 78-95.
- 946 Pardo, M., and Suarez, G. (1995) Shape of the subducted Rivera and Cocos plates in southern
947 Mexico: Seismic and tectonic implications. *Journal of Geophysical Research*, 100,
948 12357-12373.
- 949 Peláez Gaviria, J.R., Mortera Gutiérrez, C.A., Bandy, W.L., and Michaud, F. (2013) Morphology
950 and magnetic survey of the Rivera-Cocos palte boundary of Colima, Mexico. *Geofísica*
951 *Internacional*, 52, 73-85.
- 952 Petrone, C.M. (2010) Relationship between monogenetic magmatism and stratovolcanoes in
953 western Mexico: The role of low-pressure magmatic processes. *Lithos*, 119, 585-606.
- 954 Petrone, C.M., Francalanci, L., Carlson, R.W., Ferrari, L., and Conticelli, S. (2003) Unusual
955 coexistence of subdcution-related and intraplate-type magmatism: Sr, Nd and Pb isotope
956 and trace element data from the magmatism of the San Pedro-Ceboruco graben (Nayarit,
957 Mexico). *Chemical Geology*, 193, 1-24.
- 958 Picard, D., Arbaret, L., Pichavant, M., Champallier, R., and Launeau, P. (2013) The rheological
959 transition in plagioclase-bearing magmas. *Journal of Geophysical Research: Solid Earth*,
960 118, 1363-1377.
- 961 Pistone, M., Blundy, J.D., Brooker, R.A., and EIMF. (2016) Textural and chemical consequences
962 of interaction between hydrous mafic and felsic magmas: an experimental study.
963 *Contributions to Mineralogy and Petrology*, 171, 8.
- 964 Pistone, M., Caricchi, L., Ulmer, P., Burlini, L., Ardia, P., Reusser, E., Marone, F., and Arbaret,
965 L. (2012) Deformation experiments of bubble- and crystal-bearing magmas: Rheological
966 and microstructural analysis. *Journal of Geophysical Research*, 117, B05208.
- 967 Pistone, M., Caricchi, L., Ulmer, P., Reusser, E., and Ardia, P. (2013) Rheology of volatile-
968 bearing crystal mushes: Mobilization vs. viscous death. *Chemical Geology*, 345, 16-39.
- 969 Plank, and Langmuir. (1988) An evaluation of the global variations in the major element
970 chemistry of arc basalts. *Earth and Planetary Science Letters*, 90, 349-370.
- 971 Plank, T., Kelley, K.A., Zimmer, M.M., Hauri, E.H., and Wallace, P.J. (2013) Why do mafic arc
972 magmas contain ~ 4 wt% water on average? *Earth and Planetary Science Letters*, 364,
973 168-179.

- 974 Pollack, H.N. (1982) The heat flow from the continents. *Annual Reviews in Earth and Planetary*
975 *Sciences*, 10, 459-481.
- 976 Pyle, D.M., Ivanovich, M., and Sparks, R.S.J. (1988) Magma cumulate mixing identified by U-
977 Th disequilibrium dating. *Nature*, 331, 157-159.
- 978 Ramírez-Guzmán, A., Taran, Y., and Armienta, M.A. (2004) Geochemistry and origin of high-
979 pH thermal springs in the Pacific coast of Guerrero, Mexico. *Geofísica Internacional*, 43,
980 415-425.
- 981 Roberge, J., Delgado-Granados, H., and Wallace, P.J. (2009) Mafic magma recharge supplies
982 high CO₂ and SO₂ gas fluxes from Popocatepetl volcano, Mexico. *Geology*, 37, 107-110.
- 983 Rosenberg, C.L., and Handy, M.R. (2005) Experimental deformation of partially melted granite
984 revisited: implications for the continental crust. *Journal of Metamorphic Geology*, 23, 19-
985 28.
- 986 Scoates, J.S. (2000) The plagioclase-magma density paradox re-examined and the crystallization
987 of Proterozoic anorthosites. *Journal of Petrology*, 41(5), 627-649.
- 988 Shapiro, N.M., and Ritzwoller, M.H. (2004) Inferring surface heat flux distributions guided by a
989 global seismic model: particular application to Antarctica. *Earth and Planetary Science*
990 *Letters*, 223, 213-224.
- 991 Sisson, T.W., and Layne, G.D. (1993) H₂O in basalt and basaltic andesite glass inclusions from
992 four subduction-related volcanoes. *Earth and Planetary Science Letters*, 117, 619-635.
- 993 Smith, I.E.M., Stewart, R.B., Price, R.C., and Worthington, T.J. (2010) Are arc-type rocks the
994 products of magma crystallisation? Observations from a simple oceanic arc volcano:
995 Raoul Island, Kermadec Arc, SW Pacific. *Journal of Volcanology and Geothermal*
996 *Research*, 190, 219-234.
- 997 Smith, P.M., and Asimow, P.D. (2005) *Adiabat_1ph*: A new public front-end to the MELTS,
998 *pMELTS*, and *pHMELTS* models. *Geochemistry Geophysics Geosystems*, 6, Q02004.
- 999 Straub, S.M., Gomez-Tuena, A., Stuart, F.M., Zellmer, G.F., Cai, Y., and Espinasa-Perena, R.
1000 (2011) Formation of hybrid arc andesites beneath thick continental crust. *Earth and*
1001 *Planetary Science Letters*, 303, 337-347.
- 1002 Straub, S.M., Gomez-Tuena, A., Zellmer, G.F., Epinasa-Perena, R., Stuart, F., Cai, Y.,
1003 Langmuir, C.H., Martin-Del Pozzo, A.L., and Mesko, G.T. (2013) The processes of melt
1004 differentiation in arc volcanic rocks: Insights from OIB-type arc magmas in the central
1005 Mexican Volcanic Belt. *Journal of Petrology*, 54, 665-701.
- 1006 Straub, S.M., Zellmer, G.F., Gomez-Tuena, A., Epinasa-Perena, R., Martin-Del Pozzo, A.L.,
1007 Stuart, F., and Langmuir, C.H. (2014) A genetic link between silicic slab components and
1008 calc-alkaline arc volcanism in central Mexico. In A. Gomez-Tuena, S.M. Straub, and
1009 G.F. Zellmer, Eds. *Orogenic andesites and crustal growth*, 385, p. 31-64. Geological
1010 Society, London, Special Publications.
- 1011 Streck, M.J., Leeman, W.P., and Chesley, J. (2007) High-magnesian andesite from Mount
1012 Shasta: A product of magma mixing and contamination, not a primitive mantle melt.
1013 *Geology*, 35, 351-354.
- 1014 Taran, Y., Morán-Zenteno, D., Inguaggiato, S., Varley, N., and Luna-González, L. (2013)
1015 Geochemistry of thermal springs and geodynamics of the convergent Mexican Pacific
1016 margin. *Chemical Geology*, 339, 251-262.
- 1017 Tatsumi, Y. (1989) Migration of fluid phases and genesis of basalt magmas in subduction zones.
1018 *Journal of Geophysical Research*, 94, 4697-4707.

- 1019 Tepley, F.J., Davidson, J.P., and Clyne, M.A. (1999) Magmatic interactions as recorded in
1020 plagioclase phenocrysts of Chaos Crags, Lassen Volcanic Center, California. *Journal of*
1021 *Petrology*, 40(5), 787-806.
- 1022 Thorpe, R.S. (1982) Andesites: orogenic andesites and related rocks, p. 738. John Wiley & Sons.
- 1023 Turner, S.J., and Langmuir, C.H. (2015a) The global chemical systematics of arc front
1024 stratovolcanoes: Evaluating the role of crustal processes. *Earth and Planetary Science*
1025 *Letters*, 422, 182-193.
- 1026 -. (2015b) What processes control the chemical compositions of arc front volcanoes?
1027 *Geochemistry Geophysics Geosystems*, 16, 1865–1893.
- 1028 Ulmer, P. (2001) Partial melting in the mantle wedge - the role of H₂O in the genesis of mantle-
1029 derived 'arc-related' magmas. *Physics of the Earth and Planetary Interiors*, 127, 215-232.
- 1030 van der Werff, J.C., de Kruif, C.G., Blom, C., and Mellema, J. (1989) Linear viscoelastic
1031 behaviour of dense hard-sphere dispersions. *Physical Review A*, 39, 795-807.
- 1032 Vance, J.A. (1969) On synneusis. *Contributions to Mineralogy and Petrology*, 24, 7-29.
- 1033 Vance, J.A., and Gilreath, J.P. (1967) The effect of synneusis on phenocryst distribution patters
1034 in some porphyritic igneous rocks. *American Mineralogist*, 52, 529-536.
- 1035 Verma, S.P., and Luhr, J.F. (2010) Sr, Nd, and Pb isotopic evidence for the origin and evolution
1036 of the Cántaro-Colima volcanic chain, Western Mexican Volcanic Belt. *Journal of*
1037 *Volcanology and Geothermal Research*, 197, 33-51.
- 1038 Vernon, R.H. (2004) *A Practical Guide to Rock Microstructure*. viii + 594 p. Cambridge
1039 University Press, Cambridge, New York, Melbourne, Madrid, Cape Town, Singapore,
1040 Sao Paulo, Delhi.
- 1041 Vigouroux, N., Wallace, P.J., and Johnson, E.R. (2007) Sulfur speciation and oxygen fugacity in
1042 primitive magmas from the Trans-Mexican Volcanic Belt. AGU Fall Meeting, p. abstract
1043 #V41D-0795, San Francisco.
- 1044 Vigouroux, N., Wallace, P.J., and Kent, A.J.R. (2008) Volatiles in high-K magmas from the
1045 western Trans-Mexican Volcanic Belt: evidence for fluid fluxing and extreme enrichment
1046 of the mantle wedge by subduction processes. *Journal of Petrology*, 49, 1589-1618.
- 1047 Waters, L.E., and Lange, R.A. (2015) An updated calibration of the plagioclase-liquid
1048 hygrometer-thermometer applicable to basalts through rhyolites. *American Mineralogist*,
1049 100, 2172-2184.
- 1050 Whittington, A.G., Hellwig, B.M., Behrens, H., Joachim, B., Stechern, A., and Vetere, F. (2008)
1051 The viscosity of hydrous dacitic liquids: implications for the rheology of evolving silicic
1052 magmas. *Bulletin of Volcanology*, 71, 185-199.
- 1053 Yoder, H.S., Stewart, D.B., and Smith, J.R. (1957) Ternary feldspars. *Carnegie Institution of*
1054 *Washington Year Book*, 56, 206-214.
- 1055 Yogodzinski, G.M., Kay, R.W., Volynets, O.N., Koloskov, A.V., and Kay, S.M. (1995)
1056 Magnesian andesite in the western Aleutian Komandorsky region: Implications for slab
1057 melting and processes in the mantle wedge. *Geological Society of America Bulletin*,
1058 107(5), 505-519.
- 1059 Yogodzinski, G.M., Lees, J.M., Churikova, T.G., Dorendorf, F., Woerner, G., and Volynets,
1060 O.N. (2001) Geochemical evidence for the melting of subducting oceanic lithosphere at
1061 plate edges. *Nature*, 409, 500-504.
- 1062 Zellmer, G.F. (2008) Some first order observations on magma transfer from mantle wedge to
1063 upper crust at volcanic arcs. In C. Annen, and G.F. Zellmer, Eds. *Dynamics of crustal*
1064 *magma transfer, storage and differentiation*, 304, p. 15-31. Geological Society, London.

- 1065 -. (2009) Petrogenesis of Sr-rich adakitic rocks at volcanic arcs: insights from global variations
1066 of eruptive style with plate convergence rates and surface heat flux. *Journal of the*
1067 *Geological Society*, 166, 725-734.
- 1068 Zellmer, G.F., Edmonds, M., and Straub, S.M. (2015a) Volatiles in subduction zone magmatism.
1069 In G.F. Zellmer, M. Edmonds, and S.M. Straub, Eds. *The role of volatiles in the genesis,*
1070 *evolution, and eruption of arc magmas*, 410, p. 1-17. Geological Society, London, Special
1071 Publications.
- 1072 Zellmer, G.F., Freymuth, H., Cembrano, J.M., Clavero, J.E., Veloso, E.A.E., and Sielfeld, G.G.
1073 (2014a) Altered mineral uptake into fresh arc magmas: insights from U-Th isotopes of
1074 samples from Andean volcanoes under differential crustal stress regimes. In A. Gomez-
1075 Tuena, S.M. Straub, and G.F. Zellmer, Eds. *Orogenic andesites and crustal growth*, 385,
1076 p. 185-208. Geological Society, London, Special Publications.
- 1077 Zellmer, G.F., Hawkesworth, C.J., Sparks, R.S.J., Thomas, L.E., Harford, C., Brewer, T.S., and
1078 Loughlin, S. (2003) Geochemical evolution of the Soufrière Hills volcano, Montserrat,
1079 Lesser Antilles Volcanic Arc. *Journal of Petrology*, 44, 1349-1374.
- 1080 Zellmer, G.F., Hwang, S.-L., Sakamoto, N., Iizuka, Y., Harada, S., Kimura, J.-I., Tamura, Y.,
1081 and Yurimoto, H. (2015b) Interaction of arc magmas with subvolcanic hydrothermal
1082 systems: insights from compositions and metasomatic textures of olivine crystals in fresh
1083 basalts of Daisen and Mengameyama, Western Honshu, Japan. In G.F. Zellmer, M.
1084 Edmonds, and S.M. Straub, Eds. *The role of volatiles in the genesis, evolution and*
1085 *eruption of arc magmas*, 410, p. 219-236. Geological Society, London, Special
1086 Publications.
- 1087 Zellmer, G.F., Rubin, K.H., Miller, C.A., Shellnutt, J.G., Belousov, A., and Belousova, M.
1088 (2015c) Resolving discordant U-Th-Ra ages: constraints on petrogenetic processes of
1089 recent effusive eruptions at Tatun Volcano Group, northern Taiwan. In L. Caricchi, and
1090 J.D. Blundy, Eds. *Chemical, physical and temporal evolution of magmatic systems*, 422,
1091 p. 175-188. Geological Society, London, Special Publications.
- 1092 Zellmer, G.F., Sakamoto, N., Iizuka, Y., Miyoshi, M., Tamura, Y., Hsieh, H.-H., and Yurimoto,
1093 H. (2014b) Crystal uptake into aphyric arc melts: insights from two-pyroxene pseudo-
1094 decompression paths, plagioclase hygrometry, and measurement of hydrogen in olivines
1095 from mafic volcanics of southwest Japan. In A. Gomez-Tuena, S.M. Straub, and G.F.
1096 Zellmer, Eds. *Orogenic andesites and crustal growth*, 385, p. 161-184. Geological
1097 Society, London, Special Publications.
- 1098 Zellmer, G.F., Sakamoto, N., Matsuda, N., Iizuka, Y., Moebis, A., and Yurimoto, H. (2016) On
1099 progress and rate of the peritectic reaction $Fo + SiO_2 \rightarrow En$ in natural andesitic arc
1100 magmas. *Geochimica et Cosmochimica Acta*, in press.
- 1101 Zellmer, G.F., and Turner, S.P. (2007) Arc dacite genesis pathways: evidence from mafic
1102 enclaves and their hosts in Aegean lavas. *Lithos*, 95, 346-362.
- 1103

1104 **Figure Captions**

1105

1106 **Figure 1:**

1107 Map showing the crustal thickness along the Mexican Volcanic Belt (colored contours, in
1108 km), modified after Ferrari et al. (2012). Stippled lines indicate the boundaries between the
1109 Western, Central, Eastern, and Easternmost sections of the belt. Also indicated are subduction
1110 velocities along the trench (arrows, in mm yr^{-1}), after Bird (2003), and the age of the subducting
1111 plate, as given by Ferrari et al. (2012), with exception of the age at the Rivera-Cocos plate
1112 boundary that was down-corrected to 3 Ma based on a recent magnetic survey of the area (Peláez
1113 Gaviria et al., 2013); see also Bird (2003). The prominent stratovolcanoes along the belt are
1114 indicated by white triangles, based on the geological map of Gómez-Tuena et al. (2007b).
1115 Sample locations of the mafic rocks investigated as part of this study are labeled and indicated by
1116 black diamonds.

1117

1118 **Figure 2:**

1119 (a-c) Backscattered electron images and (d-e) FE-EPMA maps, displaying representative
1120 petrographic features of the mafic samples here studied, with warmer colors indicating higher
1121 concentrations. (a) Glomerocrysts of various sizes set in a plagioclase-dominated groundmass;
1122 Amatlán de Cañas sample JAL05-16. Inset depicts one of the larger glomerocrysts labeled with
1123 mineral phases olivine (ol), pyroxene (px), magnetite (mt), and interstitial plagioclase (pl). (b)
1124 Small glomerocrysts set in a plagioclase-dominated groundmass; Los Atlixcos sample PS99-
1125 20B, Palma Sola area. (c) Subhedral crystals of magnesian olivine with spinel (sp) inclusions,
1126 and euhedral to subhedral crystals of zoned pyroxene, set in a fine-grained groundmass;
1127 Zitácuaro sample ZIT99-7. Insets shows magnesian pyroxene core overgrown by a slightly more

1128 ferrous mantle of variable width, which includes an olivine in contact with the groundmass. Note
1129 that the Fe-rich overgrowth rim on this olivine is seen at the transition to the groundmass, but not
1130 in contact with the pyroxene mantle. (d) Fe-map (left) and Ca-map (right) showing anhedral to
1131 subhedral crystals of olivine and plagioclase in a groundmass dominated by low-Ca plagioclase;
1132 Los Atlixcos sample PS99-22, Palma Sola area. Concentric but complex zoning is displayed by
1133 the core of the broken plagioclase crystal. Note the isolated small calcic plagioclase crystal in the
1134 groundmass. (e) Fe-map (left) and Ca-map (right) showing subhedral crystals of olivine and
1135 plagioclase in a groundmass dominated by plagioclase and clinopyroxene; El Esquilon sample
1136 PS99-1, Palma Sola area. This sample is typical in that most plagioclase crystals are unzoned or
1137 normally zoned with unzoned cores. Note again a glomerocrysts of several lath-shaped
1138 plagioclase crystals and one olivine crystal on the right side of each image.

1139

1140 **Figure 3:**

1141 (a) Forsterite (Fo) contents of olivine crystals, microlites (less than $\sim 20\text{-}30\ \mu\text{m}$ in width, ●)
1142 and phenocrysts (more than $\sim 20\text{-}30\ \mu\text{m}$ in width, ×), compared across all samples. Samples are
1143 ordered from left to right according to decreasing western longitude. Sample names on the
1144 bottom, associated volcanic vents at the top. Vertical lines divide the Western Mexican Volcanic
1145 Belt (MVB), the Colima Volcanic Centre (VC) on the boundary between Western and Central
1146 MVB, the Central MVB, the Eastern MVB, and the Easternmost MVB.

1147

1148 **Figure 4:**

1149 (a) Mg# ranges for clinopyroxene crystals, compared across all clinopyroxene-bearing
1150 samples, with symbols as in Figure 3. Only pyroxenes with more than 90% Wo + En + Fs are

1151 plotted, and the amount of Fe^{2+} is based on the site attribution scheme of Lindsley (1983). (b)
1152 Single-pyroxene thermometry based on the Ca-content of the clinopyroxene crystals in (a), using
1153 the parameterization of Lindsley (1983) at a fixed pressure of 500 MPa. Samples are ordered
1154 with from left to right according to decreasing western longitude, as in Figure 3. See text for
1155 discussion.

1156

1157 **Figure 5:**

1158 Anorthite (An) contents of plagioclase crystals, compared across all samples, with symbols as
1159 in Figure 3; calculated as $\text{An} = \text{molar Ca}/(\text{Ca}+\text{Na}+\text{K})$. Samples are ordered from left to right
1160 according to decreasing western longitude, as in Figure 3. Labels for MVB segments are omitted
1161 here for clarity. Typical plagioclase compositions of mid-ocean ridge basalts (MORB) are
1162 indicated (cf. Kohut and Nielsen, 2003).

1163

1164 **Figure 6:**

1165 Relationship between plagioclase An content and liquid An# in equilibrium for the H_2O -
1166 saturated (grey field) and dry experiments (black field) of Waters and Lange (2015).
1167 Superimposed are ranges in An content of plagioclase phenocrysts from this study, at their
1168 respective whole-rock (i.e. ~ liquid) An# (red bars). The overlap of data ranges with the dry
1169 experiments suggests that most crystals are not in equilibrium with hydrous mafic arc melts.
1170 Rather, if formed from hydrous melts, as indicated by hydrous melt inclusions in Mexican arc
1171 samples, the liquid An# of their equilibrium melts must have ranged to much lower values (down
1172 to An_{-10}), i.e. crystals would have formed from much more evolved melts than those they are
1173 carried in.

1174

1175 **Figure 7:**

1176 An_{max} -MELTS pressure estimates: MELTS isobaric fractional crystallization models showing
1177 the An contents of the first plagioclase crystal formed at a range of pressures (■). Anhydrous
1178 melt compositions at the onset of plagioclase crystallization vary from basaltic at low pressure to
1179 dacitic at high pressure. Plagioclase microlites (●) are tagged to the MELTS trends at the low
1180 pressure end of the diagram such that the highest measured An content coincides with the
1181 MELTS trend, where possible. Phenocrysts (×) are tagged to the MELTS trend in a similar
1182 manner, at higher pressures. Uncertainties depend on how accurately the crystals can be tagged
1183 to the MELTS trends (cf. Table 5). Dashed lines represent bulk rock An#, cf. Table 2. See text
1184 for discussion.

1185

1186 **Figure 8:**

1187 Comparison of the evolving melt H₂O contents predicted for sample NAY31 between
1188 alphaMELTS isobaric crystal fractionation at NNO+1, plagioclase hygrometry (Waters and
1189 Lange, 2015), and a recent H₂O-CO₂ solubility model (Papale et al., 2006) assuming no CO₂
1190 present in the residual melt. It appears that the MELTS model returns reliable melt H₂O contents
1191 within the experimentally calibrated H₂O range, up to mid crustal pressures of ~ 300 MPa.

1192

1193 **Figure 9:**

1194 (a) Magma ponding pressures derived from the An_{max} -MELTS pressure sensor (cf. Figure 7
1195 and Figure S2) versus longitude along the Mexican Volcanic Belt. (b) Initial H₂O content of the
1196 magmas assuming that they leave the Moho at their liquidi and ascend adiabatically until they

1197 stall when degassing-induced crystallization commences. Open symbols are excluded from the
1198 correlation: sample S2 is the most evolved of the studied suite, plotting close to the basaltic
1199 andesite – andesite divide; MG05-16B is from the backarc. Boxes in (b) show H₂O
1200 determinations by hygrometry in the western TMVB (Díaz-Bravo et al., 2014) and maximum
1201 H₂O values measured in olivine melt inclusions in the rest of the arc, compiled by Plank et al.
1202 (2013) from sources cited in the text. See text for discussion.

1203

1204 **Figure 10:**

1205 (a) Total surface heat flux at the eruption sites calculated through bilinear interpolation of the
1206 global surface heat flux model of Shapiro and Ritzwoller (2004), versus ponding pressure
1207 derived using the An_{max}-MELTS pressure sensor (cf. Figure 7 and Figure S2). In (b), only the
1208 advected component of the surface heat flux is plotted. See text for discussion and caption of
1209 Figure 9 for an explanation on samples S2 and MG05-16B, which are excluded from the
1210 correlations.

1211

1212 **Figure 11:**

1213 Cartoon showing the petrogenetic model of magma ascent, magma-mush formation upon
1214 degassing, and occasional eruption of antecryst-bearing basalts from the TMVB, with surface
1215 heat flux controlled by the depth of unerupted magma-mush reservoirs. Adapted from Zellmer
1216 (2009) and Zellmer et al. (2015b).

1217

1218 **Figure S1:**

1219 Total alkali versus silica (TAS) diagram of the whole rock samples studied in this
1220 contribution. Note that most samples are basalts, trachybasalts, or silica-poor basaltic andesites.
1221 Outliers are labeled with their sample numbers. We note that the two alkaline outliers do not
1222 contain plagioclase, and the two silica-rich basaltic andesites contain orthoclase.

1223

1224 **Figure S2a-f:**

1225 An_{max} -MELTS pressure estimates. See caption of Figure 7 for details. One sample (cf. panel
1226 e) displays higher An contents than expected (indicated by question marks), and thus does not
1227 lend itself to pressure estimation.

1228

1229 **Figure S2g-l:**

1230 An_{max} -MELTS pressure estimates. See caption of Figure 7 for details. Two samples (cf.
1231 panels i and l) display higher An contents than expected (indicated by question marks), and thus
1232 do not lend themselves to pressure estimations.

1233

1234 **Figure S2m-r:**

1235 An_{max} -MELTS pressure estimates. See caption of Figure 7 for details. Two samples (cf.
1236 panels p and q) display higher An contents than expected (indicated by question marks), and thus
1237 do not lend themselves to pressure estimations.

1238

1239 **Figure S3:**

1240 An_{max} -MELTS pressure estimate of sample ZIT99-7, with 10% crystallinity, reproduced from
1241 Figure S2j. (a) Added is the MELTS same melts model run at NNO+0.5 instead of NNO+1 as an
1242 fO_2 sensitivity test (red diamonds). The An_{max} -MELTS pressure estimates are close and partially
1243 overlap. This shows that half a log-unit change in oxygen fugacity has no significant effect on
1244 the predicted plagioclase compositions. (b) Added is the MELTS model of the groundmass (blue
1245 diamonds), assuming that the crystallinity of this sample is due to equal proportions of olivine
1246 and pyroxene with the average mineral compositions of these phases in this sample. The An_{max} -
1247 MELTS pressure estimates are close and partially overlap. This shows that for samples with low
1248 crystallinity, whole rock compositions may be used instead of groundmass compositions for
1249 An_{max} -MELTS pressure estimation, with errors within as little as a few tens of MPa.

1250

1251 **Figure S4:**

1252 An -MELTS pressure estimates for Toxlacuaya (CP-49) and Rio Naolinco (CP-98) deposits of
1253 the El Vocancillo paired vent (Carrasco-Núñez et al., 2005). MELTS isobaric fractional
1254 crystallization models show the An contents of the first plagioclase crystal formed at a range of
1255 pressures (■), as in Figure 7 and Figure S2. Anhydrous melt compositions at the onset of
1256 plagioclase crystallization vary from basaltic at low pressure to dacitic at high pressure. Average
1257 plagioclase phenocryst compositions (×) of each deposit are tagged to the respective MELTS
1258 trends such that the An content coincides with the MELTS trend. As these are averages, not
1259 maxima, pressures are likely slight overestimates. Irrespectively, both flows return very similar
1260 pressures at around 700 MPa, despite their very different bulk compositions. See main text for
1261 discussion.

1262

1263 **Figure S5:**

1264 Crystallization rate is predicted to increase upon H₂O saturation and degassing. The
1265 alphaMELTS example shown here is for a short pressure interval of equilibrium crystallization
1266 of olivine during adiabatic decompression of composition NAY31 with initially 5.7 wt% H₂O
1267 and starting P-T conditions of 677 MPa and 1260°C, at NNO+1.

1268

Figure 1

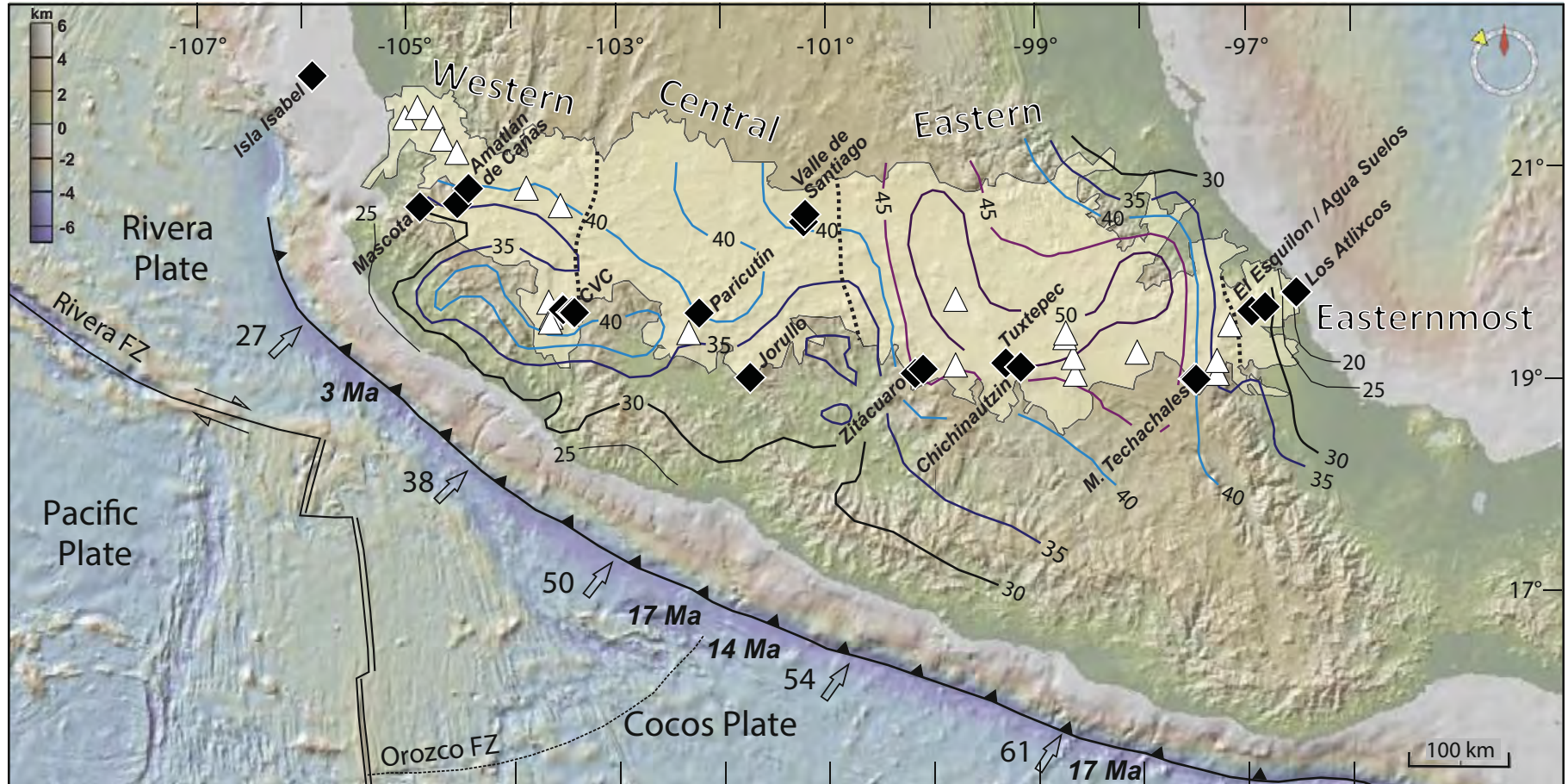


Figure 2

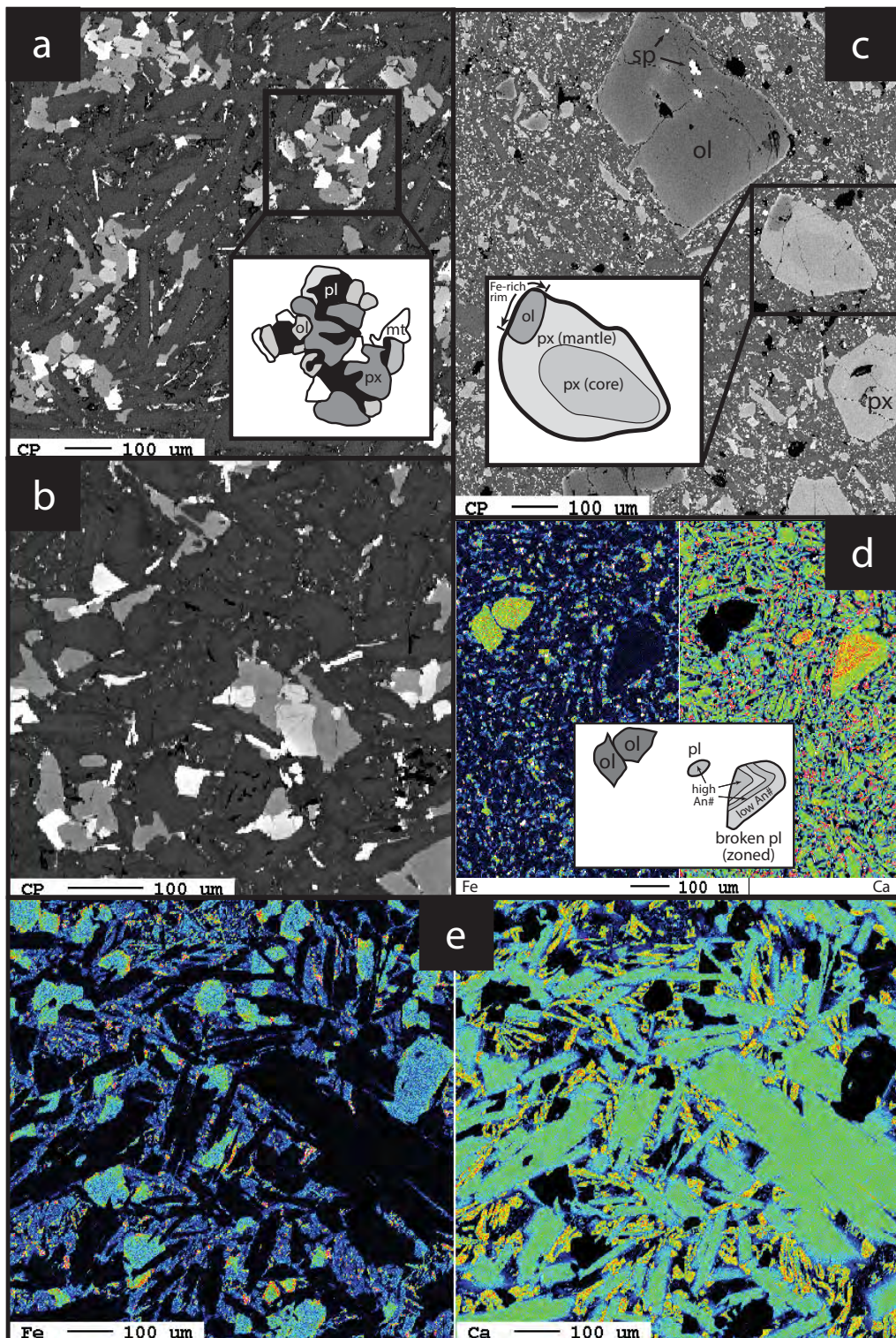


Figure 3

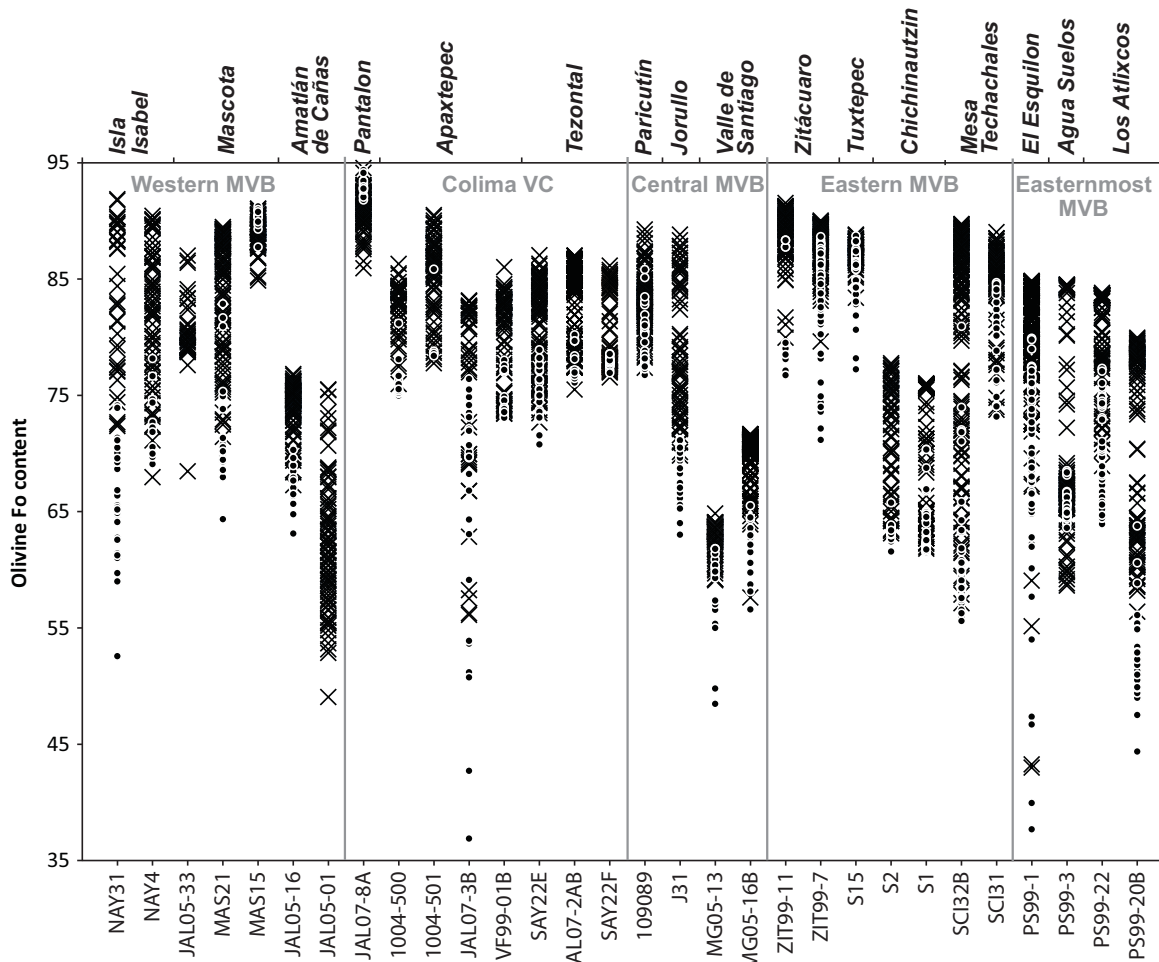


Figure 4

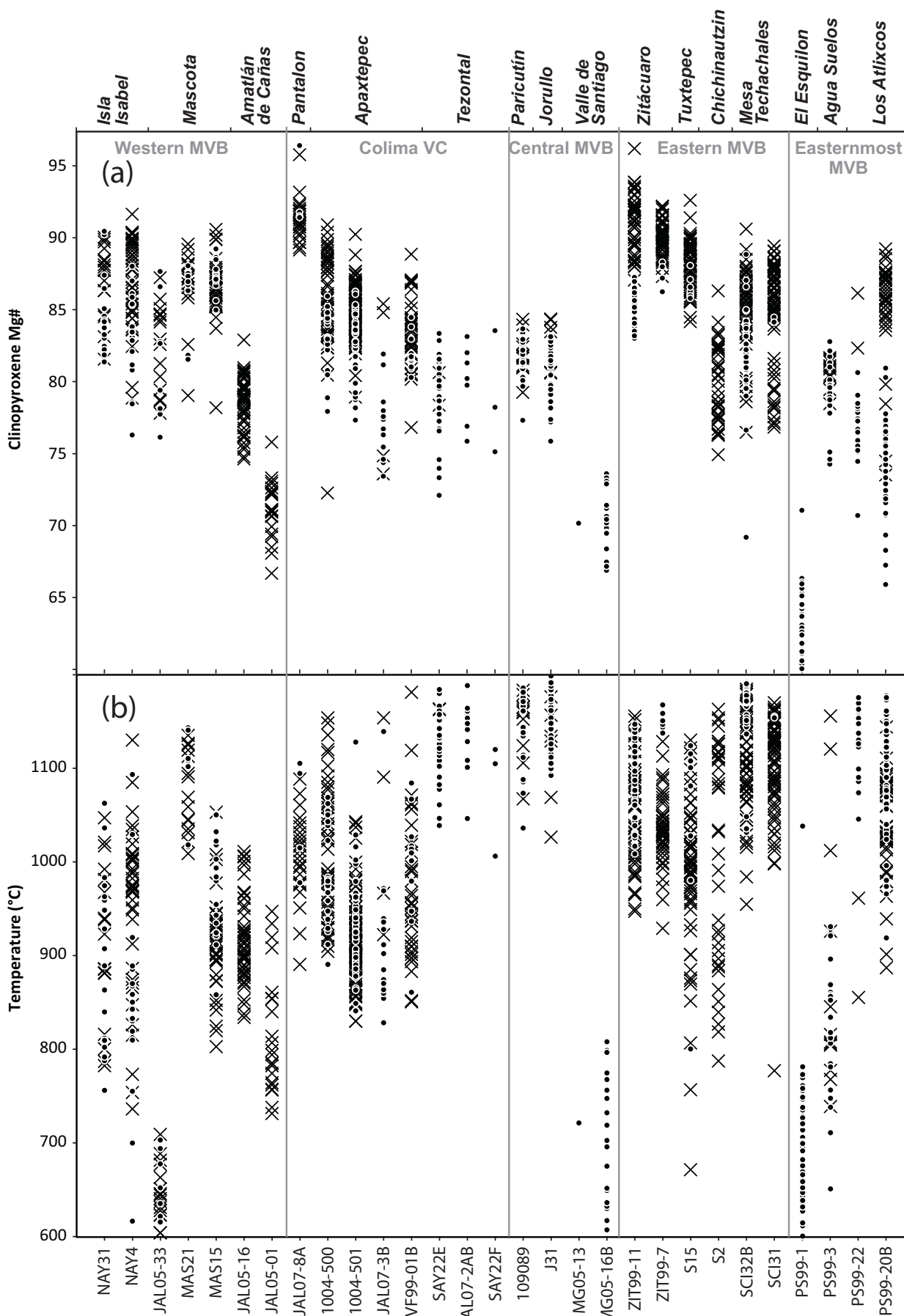


Figure 5

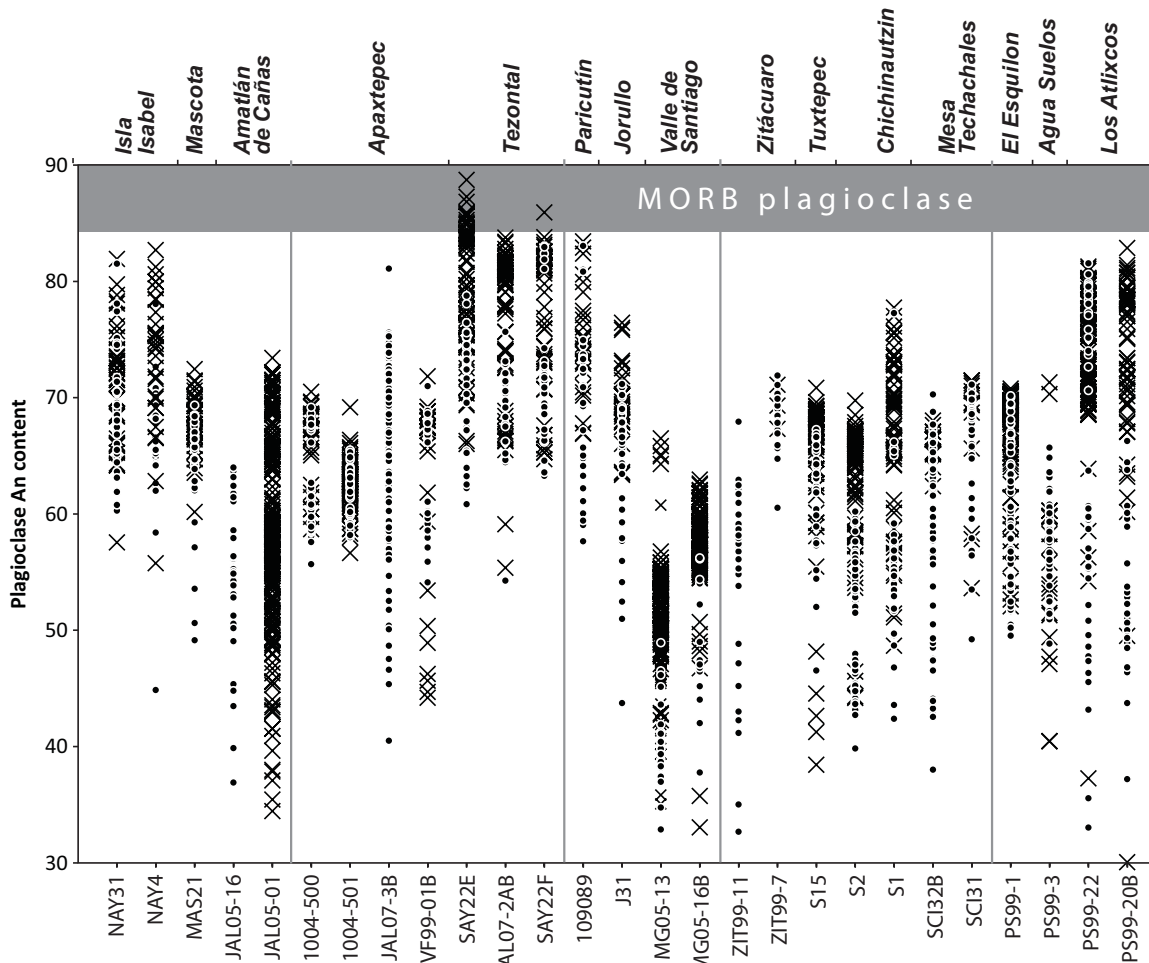


Figure 6

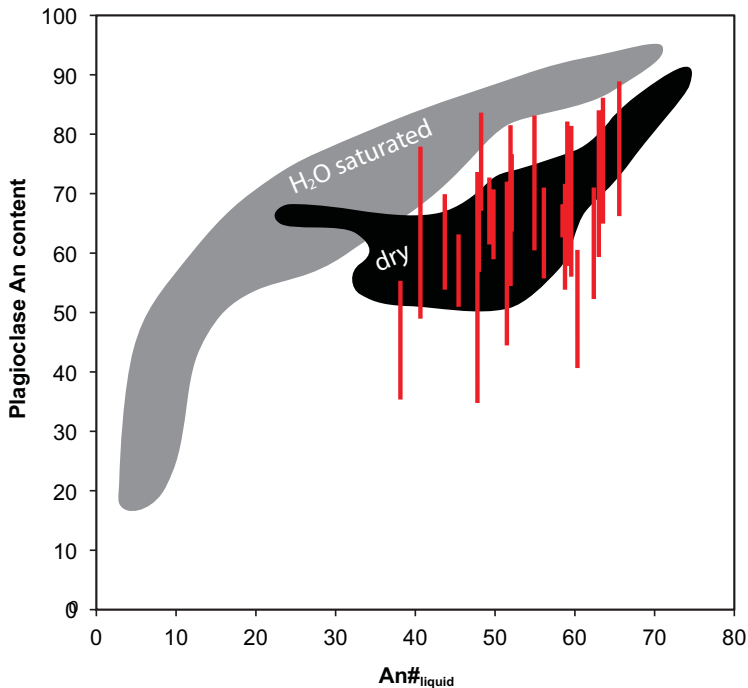


Figure 7

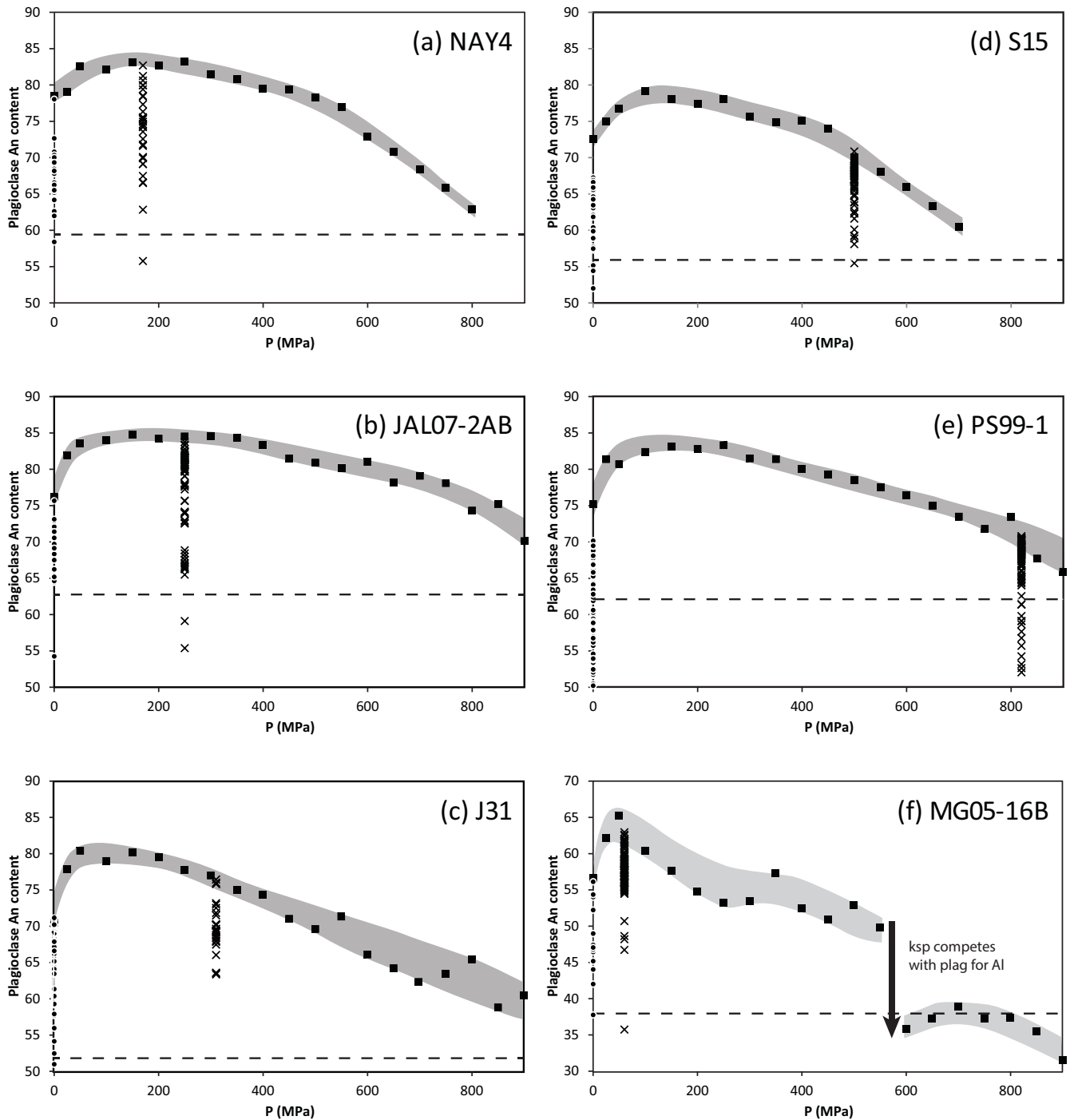


Figure 8

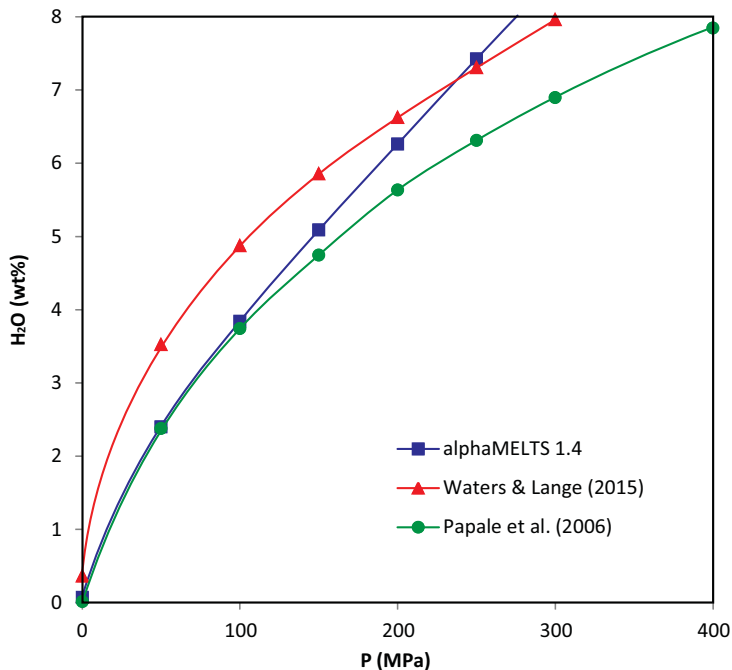


Figure 9

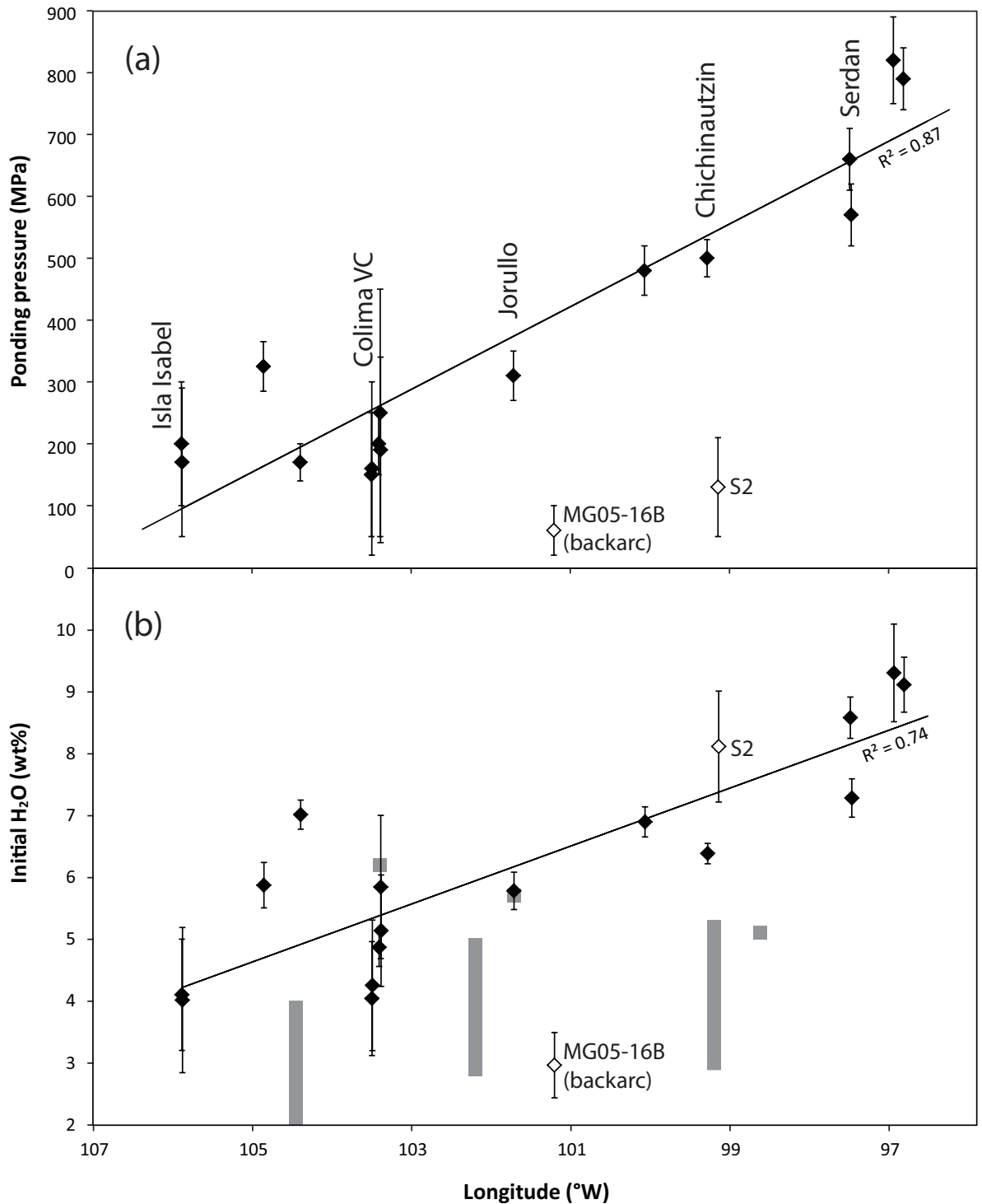


Figure 10

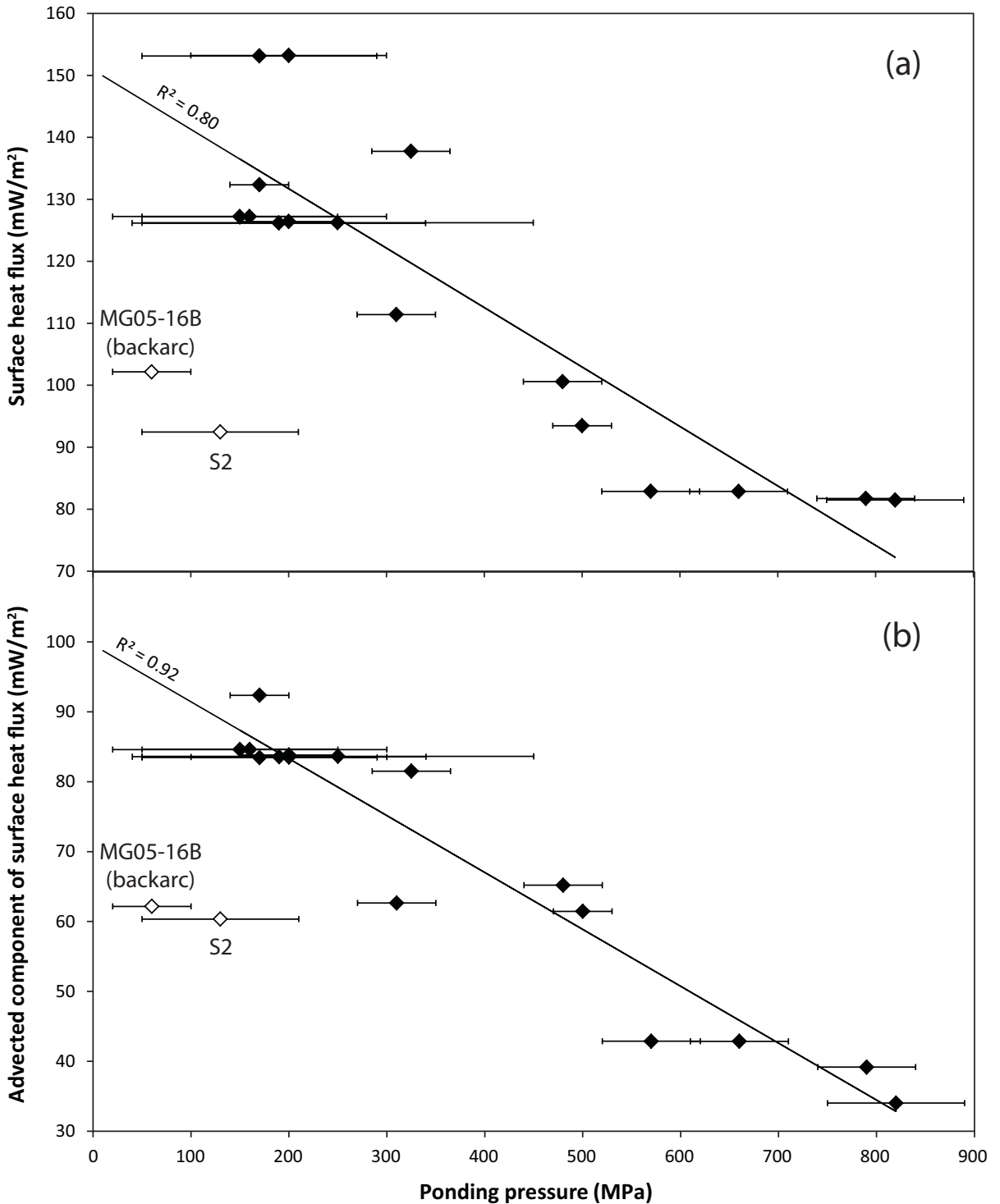


Figure 11

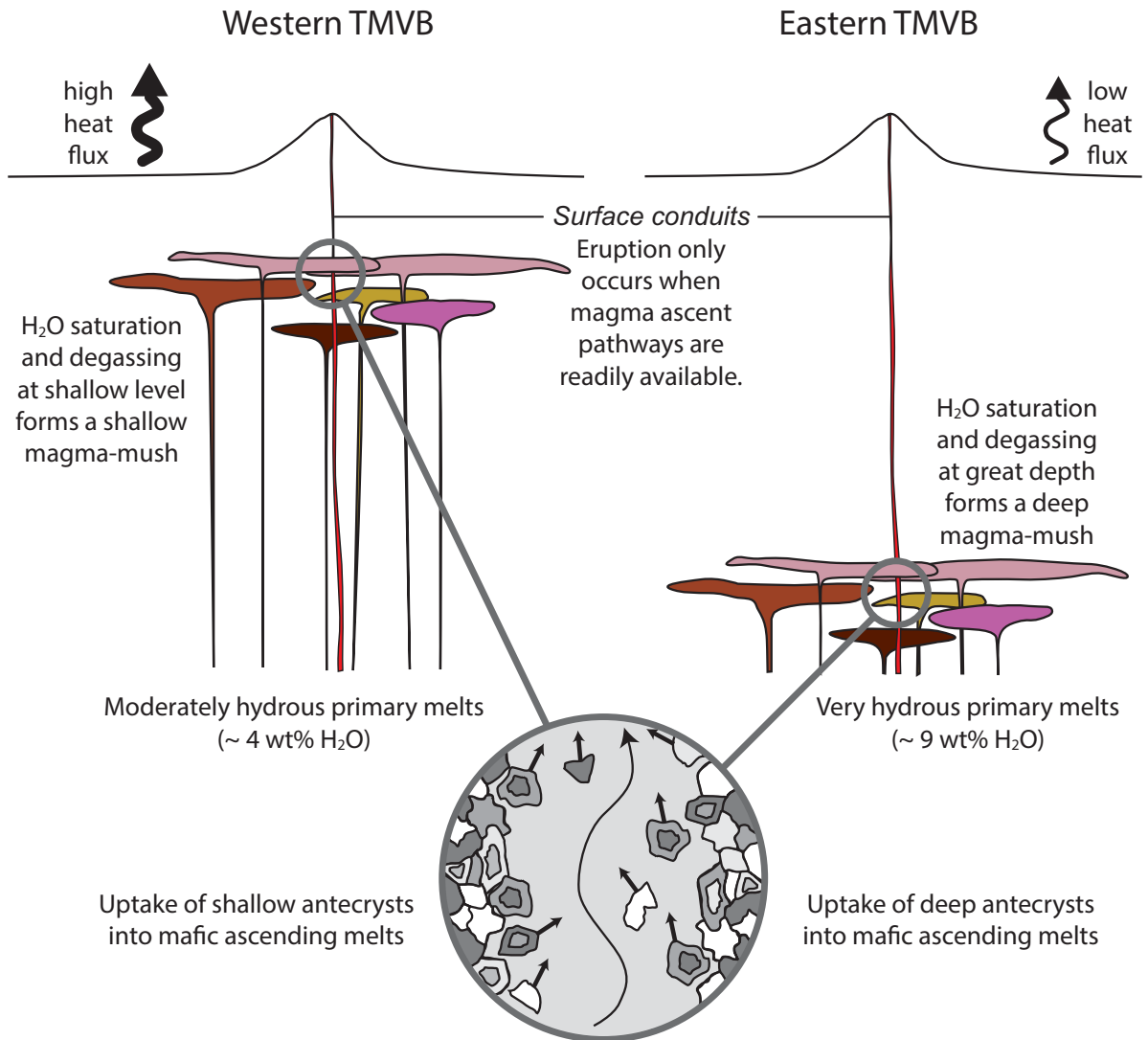


Table 1: Sample details

Name	NMNH #	Lat (°N)	Lon (°W)	Sampling site	Suite	Reference	Phenocrysts (%)
NAY31	117623-30	21.848	105.888		Isla Isabel	1	5
NAY4	117623-4	21.850	105.882		Isla Isabel	1	5
JAL05-33	-	20.565	104.860		Mascota	2	10
MAS21	117626-24	20.606	104.858		Mascota	3	< 3
MAS15	117626-18	20.542	104.708		Mascota	3	< 3
JAL05-16	-	20.639	104.504		Amatlán de Cañas	2	< 3
JAL05-01	-	20.782	104.395		Amatlán de Cañas	2	< 3
JAL07-8A	-	19.660	103.753	Pantalon	Colima Volcanic Complex	2	10
1004-500	116597-24	19.640	103.500	Apaxtepec	Colima Volcanic Complex	4	5
1004-501	116597-25	19.640	103.500	Apaxtepec	Colima Volcanic Complex	5	< 3
JAL07-3B	-	19.632	103.495	Apaxtepec	Colima Volcanic Complex	2	< 3
VF99-01B	117593-396	19.632	103.495	Apaxtepec	Colima Volcanic Complex	6	< 3
SAY22E	116597-9	19.610	103.410	Tezontal	Colima Volcanic Complex	5	< 3
JAL07-2AB	-	19.604	103.389	Tezontal	Colima Volcanic Complex	2	< 3
SAY22F	117593-226	19.605	103.385	Tezontal	Colima Volcanic Complex	6	10
109089	109089	19.600	102.200	Paricutín	Michoacán-Guanajuato	7	5
J31	116595-22	18.990	101.715	Jorullo	Michoacán-Guanajuato	8	< 3
MG05-16B	-	20.465	101.206	Valle de Santiago	Michoacán-Guanajuato	9	< 3
MG05-13	-	20.537	101.191	Valle de Santiago	Michoacán-Guanajuato	9	15
ZIT99-11	-	19.031	100.143		Valle de Bravo-Zitácuaro	10	< 3
ZIT99-7	-	19.070	100.069		Valle de Bravo-Zitácuaro	10	10
S15	-	19.128	99.281	Tuxtepec	Chichinautzin	11	< 3
S2	-	19.089	99.143	Chichinautzin	Chichinautzin	12	5
S1	-	19.088	99.138	Chichinautzin	Chichinautzin	12	10
SCI32B	-	18.980	97.489	W. Mesa Techachales	Serdan	13	10
SCI31	-	18.975	97.469	E. Mesa Techachales	Serdan	13	< 3
PS99-1	-	19.623	96.940	El Esquilon	Palma Sola	14	15
PS99-3	-	19.661	96.813	Agua Suelos	Palma Sola	14	< 3
PS99-22	-	19.795	96.519	Los Atlixcos	Palma Sola	14	5
PS99-20B	-	19.801	96.517	Los Atlixcos	Palma Sola	14	10

References:

- 1: Housh et al. (2010)
- 2: Gomez-Tuena et al. (2011)
- 3: Luhr et al. (1989)
- 4: Luhr & Carmichael (1981)
- 5: Verma & Luhr (2010)
- 6: Maria & Luhr (2008)
- 7: Hochstadter et al (1996)
- 8: Luhr & Carmichael (1985)
- 9: Ortega-Gutierrez et al. (2014)
- 10: Gomez-Tuena et al. (2007)
- 11: Straub et al. (2014)
- 12: Straub et al. (2013)
- 13: LaGatta (2003)
- 14: Gomez-Tuena et al. (2003)

Table 2: Whole rock major oxides with total Fe expressed as FeO

Name	SiO ₂	TiO ₂	Al ₂ O ₃	FeO ^T	MnO	MgO	CaO	Na ₂ O	K ₂ O	P ₂ O ₅	An# _{WR}
NAY31	48.64	1.54	16.05	7.81	0.16	10.22	10.93	3.21	1.44	0.40	58.9
NAY4	47.89	1.54	16.03	8.74	0.16	10.02	10.95	3.14	1.43	0.42	59.4
JAL05-33*	48.16	1.80	13.29	8.88	0.09	6.49	9.49	2.50	6.79	1.80	42.6
MAS21	53.34	0.82	16.80	6.99	0.12	8.09	8.45	4.10	1.01	0.28	49.1
MAS15*	50.44	1.61	13.31	8.24	0.13	9.82	7.60	2.99	4.68	1.19	40.6
JAL05-16	48.83	1.89	16.18	11.91	0.15	7.05	8.24	3.28	1.09	0.50	52.9
JAL05-01	52.08	1.69	17.43	10.85	0.13	4.58	7.67	3.68	1.39	0.40	47.6
JAL07-8A*	48.83	1.20	11.16	9.19	0.13	12.85	9.27	2.09	4.19	1.10	51.0
1004-500 ^{&}	50.09	1.74	14.71	9.22	0.15	7.38	9.36	3.19	3.01	0.76	49.7
1004-501	49.23	1.59	13.44	8.47	0.15	9.75	9.02	2.95	3.67	0.98	47.8
JAL07-3B	49.58	1.68	16.40	11.86	0.14	5.23	8.99	3.36	2.17	0.59	50.6
VF99-01B	50.49	1.67	15.30	9.46	0.14	7.08	9.06	2.84	2.80	0.70	51.3
SAY22E	49.24	0.77	16.86	10.15	0.15	9.24	10.08	2.48	0.65	0.20	65.4
JAL07-2AB	49.86	0.79	16.75	11.02	0.16	8.23	9.62	2.58	0.79	0.20	62.8
SAY22F	50.08	0.85	17.16	9.75	0.15	7.97	9.65	2.59	0.69	0.20	63.3
109089	52.49	1.32 [#]	18.52 [#]	6.24 [#]	0.12 [#]	8.17	7.89 [#]	4.1 [#]	0.81	0.35 [#]	48.1
J31 ^{&}	52.72	0.88	16.85	7.67	0.13	8.46	8.33	3.68	0.79	0.17	51.9
MG05-16B	49.22	2.42	15.43	15.04	0.20	3.62	6.28	3.91	2.54	1.23	38.0
MG05-13	47.74	2.49	17.70	14.03	0.17	4.86	7.47	3.82	1.67	0.57	45.3
ZIT99-11	52.32	0.99	14.92	8.18	0.12	8.85	8.95	3.58	1.49	0.40	51.7
ZIT99-7	51.25	0.79	16.19	8.39	0.13	8.64	8.74	3.18	1.99	0.40	51.5
S15	49.82	1.00	14.77	9.67	0.14	9.66	9.73	3.18	1.51	0.51	56.0
S2 ^{&}	55.27	1.73	17.28	7.75	0.14	4.01	7.17	4.09	1.48	0.87	43.6
S1 [§]	56.24	1.47	17.72	8.26	0.13	3.22	6.55	4.32	1.40	0.63	40.5
SCI32B	51.28	1.02	15.77	9.96	0.14	7.95	9.60	3.12	0.95	0.20	58.3
SCI31	50.77	1.02	15.68	10.12	0.14	8.48	9.57	3.08	0.92	0.22	58.6
PS99-1	48.30	1.55	16.39	12.48	0.16	8.21	9.42	2.75	0.56	0.19	62.2
PS99-3	48.49	2.08	15.93	11.78	0.16	6.63	10.24	2.80	1.36	0.52	60.2
PS99-22	51.77	1.40	16.87	10.42	0.15	6.39	8.12	3.33	1.20	0.35	51.8
PS99-20B	52.93	1.41	17.20	9.87	0.14	4.85	8.82	3.25	1.09	0.29	54.8

N.B. All samples have plagioclase, clinopyroxene and oxides, unless indicated otherwise.

*Does not contain plagioclase

[&]Contains orthopyroxene and clinopyroxene

[§]Contains orthopyroxene, but not clinopyroxene

[#]extrapolated using the Paricutín whole-rock trends of Cebria et al. (2011)

Table 3: P-T conditions of primitive melts leaving the crust-mantle boundary.

H ₂ O content (wt%)		9.09	8.26	7.41	6.54	5.66	4.76	3.85	2.91	1.96	
Name	Moho depth (km)*	Moho P (MPa) [§]	liquidus temperature (°C) [#]								
NAY31	25	677	1255	1255	1255	1255	1260	1265	1270	1280	1290
NAY4	25	677	1250	1250	1250	1255	1260	1265	1270	1275	1285
MAS21	30	819	1225	1225	1225	1230	1240	1245	1260	1280	1300
JAL05-16	35	964	1200	1200	1205	1210	1220	1235	1250	1270	1290
JAL05-01	40	1111	1160	1165	1170	1185	1195	1210	1225	1240	1265
1004-500	38	1052	1225	1225	1230	1235	1240	1245	1255	1270	1295
1004-501	38	1052	1300	1300	1300	1305	1315	1320	1330	1340	1350
JAL07-3B	38	1052	1155	1155	1160	1170	1185	1195	1210	1235	1255
VF99-01B	38	1052	1215	1215	1220	1225	1230	1240	1255	1275	1300
SAY22E	38	1052	1245	1245	1250	1255	1260	1270	1285	1305	1330
JAL07-2AB	38	1052	1220	1220	1230	1245	1255	1270	1285	1305	1330
SAY22F	38	1052	1215	1215	1220	1230	1240	1255	1275	1290	1315
109089	40	1111	1235	1240	1250	1260	1275	1290	1305	1325	1345
J31	33	905	1235	1235	1240	1245	1250	1265	1280	1300	1325
MG05-16B	40	1111	1160	1165	1165	1160	1175	1195	1250	1340	1410
MG05-13	40	1111	1160	1160	1165	1175	1180	1195	1210	1230	1250
ZIT99-11	45	1258	1265	1265	1275	1290	1300	1315	1335	1355	1375
ZIT99-7	45	1258	1265	1265	1270	1280	1295	1310	1325	1345	1370
S15	50	1406	1295	1295	1295	1300	1315	1330	1345	1365	1390
S2	50	1406	1190	1195	1205	1215	1230	1240	1260	1305	1375
S1	50	1406	1165	1170	1180	1195	1205	1220	1235	1255	1290
SCI32B	40	1111	1225	1225	1230	1245	1255	1270	1285	1305	1330
SCI31	40	1111	1240	1240	1240	1250	1260	1275	1295	1315	1335
PS99-1	32	876	1215	1215	1215	1220	1225	1230	1245	1260	1285
PS99-3	31	1023	1180	1180	1180	1185	1195	1210	1225	1245	1265
PS99-22	20	537	1165	1165	1165	1165	1170	1175	1180	1195	1220
PS99-20B	20	537	1100	1100	1100	1100	1110	1120	1135	1155	1175

*Estimated from Figure 1

[§]Using the crustal density structure of Ortega-Gutierrez et al. (2014) down to 32 km below the surface, and 3 g/cm³ from 32 km to the Moho

[#]Modeled through MELTS at an oxygen fugacity 1 log unit above the NNO buffer (cf. Vigouroux et al., 2008)

Table 4: Pressures of degassing-induced crystallization during adiabatic ascent from the Moho

H ₂ O content (wt%)	9.09	8.26	7.41	6.54	5.66	4.76	3.85	2.91	1.96
Name	pressures (MPa) [#]								
NAY31	587	587	577	497	367	257	167	57	7
NAY4	617	617	607	477	357	237	137	67	7
MAS21	669	609	489	379	289	209	79	9	0.1
JAL05-16	not modeled (plag microlites only)								
JAL05-01	431	331	241	111	51	1	0.1	0.1	0.1
1004-500	842	712	572	452	342	242	132	32	0.1
1004-501	not modeled (observed plag phenocryst X _{An} content too high, cf. Figure S2e)								
JAL07-3B	not modeled (plag microlites only)								
VF99-01B	822	702	572	452	342	222	82	2	0.1
SAY22E	882	762	612	472	352	182	42	0.1	0.1
JAL07-2AB	782	652	532	302	162	42	0.1	0.1	0.1
SAY22F	822	682	552	442	252	92	2	0.1	0.1
109089	not modeled (observed plag phenocryst X _{An} content too high, cf. Figure S2i)								
J31	725	645	525	405	305	155	55	0.1	0.1
MG05-16B	681	581	471	371	291	211	1	0.1	0.1
MG05-13	661	561	461	371	281	61	0.1	0.1	0.1
ZIT99-11	not modeled (plag microlites only)								
ZIT99-7	868	708	568	448	298	128	28	0.1	0.1
S15	896	786	626	486	356	146	36	0.1	0.1
S2	216	146	76	26	6	0.1	0.1	0.1	0.1
S1	not modeled (observed plag phenocryst X _{An} content too high, cf. Figure S2l)								
SCI32B	791	661	531	371	211	71	1	0.1	0.1
SCI31	841	711	571	451	301	121	11	0.1	0.1
PS99-1	756	706	596	466	356	246	76	6	0.1
PS99-3	763	673	553	443	303	113	23	0.1	0.1
PS99-22	not modeled (observed plag phenocryst X _{An} content too high, cf. Figure S2p)								
PS99-20B	not modeled (observed plag phenocryst X _{An} content too high, cf. Figure S2q)								

[#]Modeled by MELTS equilibrium crystallization modeling at an oxygen fugacity 1 log unit above the NNO buffer

Table 5: Estimated along-arc variations in some physical and chemical parameters

Name	latitude (°N)	longitude (°W)	Moho P (MPa)	initial T [§] (°C)	initial H ₂ O [#] (wt%)	±	ponding pressure* (MPa)	±	initial ponding T (°C)	Melt Density ^{&} (kg/m ³)	Log Melt Viscosity [\] (Pa s)	total heat flux [%] (mW/m ²)	advected heat flux (mW/m ²)
NAY31	21.848	105.888	677	1269	4.1	0.9	200	100	1239	2396	0.26	153	100
NAY4	21.850	105.882	677	1269	4.0	1.2	170	120	1236	2411	0.24	153	100
MAS21	20.606	104.858	819	1235	5.9	0.4	325	40	1201	2252	0.51	138	96
JAL05-01	20.782	104.395	1111	1177	7.0	0.2	170	30	1097	2388	0.98	132	105
1004-500	19.640	103.500	1052	1252	4.0	0.9	150	100	1199	2377	0.73	127	97
VF99-01B	19.632	103.495	1052	1248	4.3	1.1	160	140	1191	2365	0.77	127	97
SAY22E	19.610	103.410	1052	1269	4.9	0.3	200	50	1213	2366	0.28	126	96
JAL07-2AB	19.604	103.389	1052	1253	5.8	1.2	250	200	1189	2312	0.39	126	96
SAY22F	19.605	103.385	1052	1249	5.1	0.9	190	150	1185	2334	0.48	126	96
J31	18.990	101.715	905	1249	5.8	0.3	310	40	1208	2267	0.46	111	74
MG05-16B	20.465	101.206	1111	1320	3.0	0.5	60	40	1260	2460	0.63	102	72
ZIT99-7	19.070	100.069	1258	1275	6.9	0.2	480	40	1222	2227	0.30	101	75
S15	19.128	99.281	1406	1302	6.4	0.2	500	30	1240	2284	0.20	93	70
S2	19.089	99.143	1406	1197	8.1	0.9	130	80	1081	2103	1.13	92	69
SCI32B	18.980	97.489	1111	1222	8.6	0.3	660	50	1191	2173	0.34	83	51
SCI31	18.975	97.469	1111	1241	7.3	0.3	570	50	1202	2241	0.34	83	51
PS99-1	19.623	96.940	876	1215	9.3	0.8	820	70	1203	2180	0.16	81	42
PS99-3	19.661	96.813	1023	1180	9.1	0.4	790	50	1158	2182	0.44	82	47

[§]Derived from Table 3, using the derived initial H₂O content. Uncertainties typically less than ± 20°C.

[#]Derived from Table 4, assuming that ponding occurs when degassing-induced crystallization during adiabatic ascent commences.

*From An_{max}-MELTS barometry, cf. Figure 7 and Figure S2. Approximate uncertainties given by how accurately maximum An-contents can be tagged to the MELTS trend.

[&]Residual melt density at ponding depth calculated using the density model of Lange and Carmichael (1987), at pressure, temperature, and H₂O content in the melt conditions reported here.

[\]Residual melt viscosity at ponding depth calculated using the viscosity model of Giordano et al. (2008), not corrected for the pressure effect (Ardia et al., 2008; Hui et al., 2009; Pistone et al., 2012).

[%]Derived by bilinear interpolation of Shapiro & Ritzwoller's (2004) global model. See text for discussion of advected component.